

Multilayered Nanoclusters of Platinum and Gold: Insights on Electrodeposition Pathways, Electrocatalysis, Surface and Bulk Compositional Properties

Tumaini S. Mkwizu,^{a,b,z} Mkhulu K. Mathe,^{b,z} and Ignacy Cukrowski^{a,z}

^a Department of Chemistry, University of Pretoria, NW-1 Building, Pretoria, 0002, South Africa.

^b Materials Science and Manufacturing Unit, Council for Scientific and Industrial Research
(CSIR), P O Box 395, Pretoria, 0001, South Africa

^z E-mail: tumaini.mkwizu@tuks.co.za; kmathe@csir.co.za; ignacy.cukrowski@up.ac.za

Abstract

Electrochemical, surface and bulk compositional properties of multilayered nanoclusters of Pt and Au, electrochemically deposited on glassy carbon under conditions involving sequential surface-limited redox-replacement reactions (performed at open-circuit) and voltammetric dealloying of templating adlayers of electrodeposited Cu, have been studied in the direction of electrocatalytic applications. Variations in open-circuit potentials during redox-replacement steps indicated thermodynamically-favored formation of Pt(s) and Au(s). Unique bimetallic interfacial active sites, Pt|Au or Au|Pt, were effectively generated as evidenced by their distinct surface electrochemistry and multicomponent X-ray photoelectron spectral features. The bulk and surface-to-near surface distribution of Pt and Au appeared to be influenced by the stoichiometry of the surface redox-replacement reactions and sequential dealloying processes through which the nanoclusters were synthesized. Interactions between metal centers, carbon and oxygen containing surface functional groups on the glassy carbon appeared to have played a significant role in the overall stabilization and catalytic activity of the nanoclusters. Profound effects were also found on interfacial charge-transfer and adsorptive properties involving carbon monoxide and its subsequent electrooxidation to CO₂, as well as on the electrocatalytic activity involving formic acid oxidation reaction, where the Pt-rich (Pt|Au) exhibited the highest activity.

1. Introduction

Nanostructured materials composed of noble metals have found a great deal of attention toward their applications as electrocatalysts in energy conversion devices, optics, electronics, and electrochemical sensor technologies for detection of pollutants and biologically-important substances, among other promising nanotechnological uses.¹⁻³ In particular, nanoalloys or metal-based nanoclusters are very appealing because they typically constitute unique type of materials that have chemical and physical properties that can remarkably be distinct from those of their atomic building blocks or bulk particulate forms.^{4,5}

Platinum-based nanostructured materials find widespread applications in catalysis and electrocatalysis.⁶ Various molecular level effects on Pt-based bimetallic systems in electrocatalysis have largely been interpreted using three models, namely; (i) ensemble effects; (ii) bifunctional mechanisms, and (iii) electronic effects.^{7,8} Ensemble effects involve the role of metal adatoms in blocking surface sites for side reactions that generate poisoning species, or blocking adsorption of inhibiting species that require more than one surface site for their adsorption.^{9,10} In a bifunctional mechanism, the surface of the electrocatalyst is considered to have two types of sites that play distinct roles in the electrocatalytic reaction.¹ In bimetallic Pt-based catalytic systems, for example, Pt sites are understood to play the role of breaking bonds such as H-C of organic molecules upon adsorption, while the second metal or adatom, can adsorb oxygenated species such as O-H groups and assist in subsequent oxidation of strongly-adsorbing intermediates such as adsorbed CO (CO_{ads}).¹¹

Electronic effects are thought to come to play when there is some modification of the electronic properties of accessible surface sites of one metal and adjacent sites of a second metal, such that reactions on the surface sites proceed differently compared to the situation with an

absence of the second metal.^{7, 12, 13} Theoretically, the preceding electronic effects in metal-based catalysts can be explained using the infamous *d*-band model pioneered by Hammer and Norskov.¹⁴ The Hammer-Norskov model prescribes that the variation in adsorption energy (and hence the catalytic activity) from one metal to the next is determined by the electronic structure of the surface whereby for the transition metals the coupling between the adsorbate valence states and the metal *d*-states principally establish such variations; the tenet of the *d*-band model is that the higher in energy the *d*-states are relative to the highest occupied state — the Fermi energy — of the metal, the stronger the interaction with adsorbate states. The reason is that when the *d*-states are close to the Fermi energy, antibonding states can be shifted well above it and become empty (or bonding states can be shifted below it and become occupied), effectively increasing the bond strength. Thus, the electronic structure of a platinum surface, and in turn its overall reactivity, can be tuned by inserting another metal in its lattice and this can directly influence the oxygen and hydrogen adsorption energies due to an up-shift of the Pt surface *d*-states.¹⁵

Gold clusters have been realized to have catalytic activity for CO oxidation and, when incorporated as adatoms to Pt, they have also been demonstrated to also have a stabilizing effect on underlying Pt metal surfaces, effectively suppressing Pt dissolution under highly oxidizing conditions.¹⁶ Moreover, recent theoretical studies of clusters of the type Pt_mAu_n ($m + n = 4$), performed within the framework of Density Functional Theory (DFT), indicate that there are some underlying electronic effects that change the interaction of CO with Pt in the bimetallic systems.^{17, 18}

Since electrocatalytic reactions are structure-sensitive as determined by the composition and solid-state structure of the electrocatalyst employed, generally, synthetic challenges of multimetallic electrocatalysts include; (i) generation of well-dispersed particles and control of their sizes, (ii) efficient utilization of the catalytic material by way of increasing surface-activity

of constituent metals, (iii) maximization of synergistic effects at primary active sites, especially on bimetallic systems, and (iv) overall low fabrication costs.^{3, 19} Most conventional synthetic approaches of noble metal nanoparticulate electrocatalysts utilise reduction of metal salts in chemical baths and multiple additional purification steps and fabrication of the prepared particles to an electrode arrangement required in subsequent electrocatalytic applications.^{6, 20} These methods generally involve substantial challenges in controlling locations and compositions of electrocatalytically-active nanoparticles. Electrochemical methods inherently involve growth of nanoparticles at interfaces of conductive surfaces and the electrolyte used, and the requirement for electronic conduction is essentially maintained during subsequent electrocatalytic reactions at the active sites of the support; the same sites where electrodeposition takes place will, in principle, be active during subsequent electrocatalysis. In addition, electrochemical methods are relatively low-cost techniques.²¹

Typical electrochemical methods being exploited in synthesis and fabrication of platinum-based nanostructured systems include galvanostatic or potentiostatic routes, where the underlying nanostructures are tuned by the nature of variation of the applied deposition current or potential with deposition time; in these processes electrons and energy required to drive the deposition reactions are generated by an external source.²²⁻²⁸ In particular, potentiostatic routes can further be categorized as involving: (i) Overpotential Deposition (OPD), where a potential $E_{M^{z+}/M}$ is applied to a conductive substrate to drive reductive reaction, nucleation and growth of a solid metal phase from its corresponding metal ions, effectively with $E_{M^{z+}/M}$ more negative than the equilibrium potential, E_{eq} , of the underlying reaction; and (ii) Underpotential Deposition (UPD) whereby deposition of adatoms of a metal takes place on a foreign metal substrate at potentials that are more positive than E_{eq} of the metal ion deposition on its own metal surface, typically

producing sub-monolayer to monolayer phases of the metal.^{29, 30} Moreover, spontaneous deposition of noble metals such as ruthenium or platinum may proceed on appropriate electrodic substrates without any utilization of an external current to achieve reduction of metal ions (This method forms part of deposition techniques generally referred as Electroless Deposition in which case the reducing equivalents required are characteristically inherent on the surfaces of the substrates used).^{25, 31, 32}

Manipulation of UPD and Electroless Deposition can be exploited to synthesize various nanofilms and nanostructured Pt-based systems. For instance, Adzic and coworkers pioneered synthesis of noble metal monolayer electrocatalysts via surface-limited redox replacement (SLRR) of metal monolayers of UPD sacrificial metals on nanoparticles or single-crystal substrates, resulting in noble metal monolayer decorated catalytic materials.^{16, 33} Epitaxial monometallic ultrathin films of Platinum Group Metals (PGMs), such as Pt and Ru, have been grown via repetitive SLRR steps involving UPD Cu or Pb on crystalline gold substrates.³⁴⁻³⁶ Moreover, overpotentially-deposited Ni bilayers through SLRR reactions involving Pt on polycrystalline Au was demonstrated to be just as effective as UPD based SLRR in deposition of Pt films.³⁷

Strasser and coworkers have explored an electrosynthetic methodology to generate core-shell type of nanomaterials (dealloyed electrocatalysts) by selective dissolution of a less noble metal such as Cu, by means of an applied potential, from a bimetallic alloy such as Pt_xCu_{1-x} , proposing that some kind of competition between the dissolution process and surface diffusion of the constituent metals results in a three dimensional metal removal and restructuring of atoms inside the bulk of the alloy.^{38, 39} Galvanic replacement has also been demonstrated in fabrication of nanoporous core-shell structured noble metal-based systems in which case prefabricated base metal or alloyed systems such as Ni/Al nanorods, Cu_xAl_{100-x} , and Au_xCu_{100-x} are used in situ as

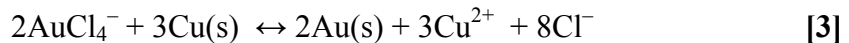
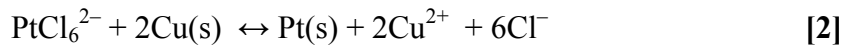
both reducing agents and three-dimensional substrates.⁴⁰⁻⁴² Obradovic and co-workers explored electrochemical studies on synergistic effects of Pt adlayers on bulk Au polycrystalline electrodes and Au adlayers on bulk polycrystalline Pt electrodes via SLRR steps involving UPD Cu⁴³; it was also observed that electronic modification of Pt by Au is insignificant on Au-modified Pt electrodes and considerable on Pt-modified Au electrodes as probed using formic acid electrocatalysis.

In our earlier works,^{44, 45} we demonstrated that unique combination of sequentially-implemented Cu UPD and OPD SLRR steps and electrochemical dealloying can be employed in synthesis of multilayered nanoclusters of Pt, Ru and Au, as monometallic or bimetallic systems supported on the carbonaceous substrate glassy carbon (GC); the nanoclusters were effectively tested as electrocatalysts for oxygen reduction and methanol oxidation reactions. In this article, we provide fresh in-depth analyses on the sequential electrochemical deposition strategies to generate the multilayered Pt and Au nanoclusters where focus has been placed on understanding the interplay of thermodynamics during growth of the nanoclusters, their resultant surface as well as bulk compositional properties, and their electrocatalytic activity with respect to CO adsorption-oxidation process and formic acid electrooxidation.

2. EXPERIMENTAL SECTION

2.1 Materials – All solutions were prepared with high-purity deionised water obtained from a Milli-Q water purifier system (Millipore Inc. USA) at resistivity of 18 MΩ·cm. All electrochemical experiments were performed in air-conditioned laboratory environment at 25 (± 1) ° C. 1 x 10⁻³ mol/L precursor electrolyte solutions of Pt⁴⁺, Au³⁺, and Cu²⁺ – dissolved in 0.1 mol/L HClO₄ used as the blank electrolyte (BE) at pH 1 ± 0.05 – were prepared from H₂PtCl₆, HAuCl₄, and CuSO₄ salts obtained from SA Precious Metals (Pty) and Merck. All chemicals were of analytical grade with at least 99% purity.

2.2 *Electrodeposition* – Substrate-immobilized monometallic or bimetallic nanostructures were synthesised in a three-electrode flow-cell connected to a custom-developed automated instrumental setup described previously;⁴⁵ the setup consisted of (i) a potentiostat/galvanostat (model PGSTAT30, Metrohm Autolab, Netherlands), (ii) a stainless steel counter electrode, (iii) the GC substrate under study (grade V-25, SPI Supplies, USA) as working electrode, and (iv) Ag/AgCl/ 3M KCl reference electrode (model 6.0727.000, Metrohm Autolab) – unless otherwise stated, potentials are reported versus (vs) this reference electrode. Nature of the noble-metal precursors was confirmed using UV-visible spectroscopy of the appropriate aqueous solutions using an Avaspec – 2048 (Avantes) spectrometer where bands due to typical ligand-to-metal charge transfer transitions in the PtCl_6^- and AuCl_4^- aquo complexes were used for confirmation of stability of the complexes in the BE according to appropriate literature.^{46, 47} Experiments were performed at $\text{pH } 1 \pm 0.05$ using 0.1 mol/L HClO_4 as BE, in line with generally known aqueous chemistry of ClO_4^- anions as non-complexing anions in the presence of noble metal cations and their non-adsorbing nature on noble metal surfaces.⁴⁸ Pre-treatment procedures of the GC substrate were as per our previous studies.⁴⁵ We have utilised sequential deposition routes involving SLRR steps and voltammetric dealloying summarised in Reactions 1–3 and Figure 1.



Steps in synthesis of bimetallic nanoclusters ${}_n(\text{M} | \text{N})_{\text{Cu}}/\text{GC}$ ($\text{M}, \text{N} = \text{Pt}$ or Au) involved six-stage deposition cycles, whereas the monometallic systems ${}_n(\text{Pt})_{\text{Cu}}/\text{GC}$ and ${}_n(\text{Au})_{\text{Cu}}/\text{GC}$ as well as the sequentially-codeposited bimetallic system ${}_n(\text{Au-Pt})_{\text{Cu}}/\text{GC}$ were generated utilising three-stage cycles. The notation $\text{M}|N$ indicate monometallic metal adlayers M and N individually deposited over each other in a sequential fashion, with N as the first deposited metal culminating

with deposition of M ; the notation ${}_n(M | N)_{Cu}/GC$ indicate a bimetallic system of n adlayers of M and N each deposited via open-circuit SLRR reactions involving Cu with glassy carbon (GC) as the substrate. Monometallic systems involving n adlayers of one noble metal are represented as ${}_n(M)_{Cu}/GC$. Rinsing steps involved the BE at a fixed potential $E = +0.2$ V, followed by injection of the Cu^{2+} solution at the same potential. Given that the standard reduction potential of the $Cu^{2+}/Cu(s)$ redox couple is 0.340 V (vs SHE) – for a 1 mmol/L Cu^{2+} solution the Nernstian equilibrium potential is approximately 0.046 V (vs Ag/AgCl/3M KCl) – sacrificial Cu(s) deposition was carried out at $E_{dep} = -0.05$ V / +0.05 V, followed by rinsing with BE at E_{dep} . Injection of the $PtCl_6^{2-}$ or $AuCl_4^-$ precursor solutions was carried out at Open-Circuit (OC), followed by the OC SLRR at quiescent conditions according to Reaction 2 or 3, respectively. Inherent in the deposition cycles was the rinsing and dealloying step at $E_{dep} = +0.2$ V during Stages 1 and 4 after Cycle 2 (see Figure 1) – steps during which voltammetric dealloying of any remaining Cu(s) to Cu^{2+} was intended to proceed according to Reaction 1. It should be understood that, in the case of the use of Cu UPD (which does not happen on pristine GC for the experimental conditions employed in this work), spontaneously formed Pt or Au during the first cycle on fresh GC determined subsequent Cu UPD cycles. Cu(s) electrodeposition stages were for 90 s as per our previous studies.⁴⁵ All solution rinsing and injection stages were performed for 20 s at 5 mL/min and all OC SLRR steps were allowed for a maximum time of 180 s. Deposition steps were repeated up to $n = 8$ cycles with respect to: (a) stepwise increase of the size of nanostructures, and (b) stepwise growth of nanostructures in relation to tuning of their electrocatalytic properties. Current-potential-time ($i-E-t$) data were sampled in situ at 0.2 s intervals.

2.3 Thermodynamic Modelling – Equilibrium models of potential-pH ($E-pH$) – Pourbaix-type multicomponent models – for Pt-Cu-H₂O, Pt-Au-H₂O, and Pt-Cu-Cl-H₂O, and Au-Cu-Cl-

H₂O systems were generated using the thermochemical software package FactSageTM (version 5.5)⁴⁹ at 298.15 K and molality of all aqueous forms of Pt, Cu, Au incorporated in the models of 1×10^{-4} mol/Kg and 1×10^{-3} mol/Kg, and molality of Cl⁻ between 1×10^{-6} mol/Kg and 1×10^{-1} mol/Kg.

2.4 Electrochemical Characterization – Post-synthesis electrochemical measurements involving Anodic Stripping Voltammetry (ASV), Cyclic Voltammetry (CV) and Electrochemical Impedance Spectroscopy (EIS) were performed with the same potentiostat/galvanostat of the deposition instrumental setup described above, but utilising commercial software packages GPES 4.9, FRA 4.9 and NOVA 1.6 (Metrohm Autolab, The Netherlands). Modelling of EIS, using equivalent circuits and complex nonlinear least-squares (CNLS) procedures, based on Boukamp's algorithms,⁵⁰ was performed with built-in data analysis modules of FRA 4.9 and NOVA 1.6. Electrochemically-active surface area (EASA) of a nanocluster electrode was estimated from ASV involving UPD Cu deposited at 0.05 V for 90s, using 1 mmol/L CuSO₄ (in 0.1 mol/L HClO₄) solution, anodically stripped at scan rate of 50 mV/s; EASA values were extracted using a conversion factor of 420 μC cm⁻² by integration of ASV peaks, after appropriate baseline subtraction, following literature methods.^{51, 52} The electrochemical behaviour of the nanocluster electrodes were characterized by means of CV in N₂-saturated 0.1 mol/L HClO₄ solution recorded at 50 mV/s from -0.2 V to +1.4 V, for 5 to 10 cycles. HCOOH electro-oxidation studies were carried out in quiescent N₂-saturated 0.5 mol/L solutions (all prepared in 0.1 mol/L HClO₄) solutions injected to the electrochemical flow-cell containing the freshly prepared immobilized nanoclusters. CV of HCOOH was ran at 50 mV/s for 5 cycles in the potential range 0 V – +1.0 V, followed by EIS measurements in freshly-injected solutions, at appropriate bias potentials between 0 and +0.4 V, using sine-wave signals of 10 mV amplitude in the frequency range 0.5 Hz – 100 kHz. CO adsorption-oxidation studies were performed using

CO-saturated 0.1 mol/L HClO₄ solution, with saturation times of at least 1800 s, after which ASV was employed to strip the adsorbed CO at scan rates between 10 mV/s and 50 mV/s from 0 V to + 1.2 V in N₂-saturated 0.1 mol/L HClO₄ solution; a single peristaltic pump (Model MINIPULS 3, GILSON S.A.S) was used to direct the gas saturated solutions to the flow-cell. In between all electrochemical measurements the flow-cell was rinsed at OC with N₂-saturated 0.1 mol/L HClO₄.

2.5 Surface and Bulk Characterization – Freshly-prepared samples were subjected to various ex-situ characterizations. Atomic Force Microscopy (AFM) using a DI Nanoscope IVa (Digital Instruments, USA) in ambient tapping mode using a model RTESPW tip (Veeco Manufacturing, USA) provided additional in-depth morphological and topographical characteristics of the nanoclusters. X-ray Photoelectron Spectroscopy (XPS) measurements were performed with a PHI spectrometer (model 5400), equipped with a non-monochromatic magnesium K_α X-ray source (1253.6 eV, operated at 15 kV and 300 W in ultra-high vacuum chamber with base pressure < 1 x 10⁻⁸ Torr) and a concentric hemispherical sector analyzer. The spectra were recorded at scan rate of 0.16 eV s⁻¹ (step-size of 0.05 eV) and take-off angle of 45°. The spectrometer was calibrated using Au and Cu standards' peaks of Au 4f_{1/2} (84.0 eV), Cu 2p_{1/2} (953 eV) and Cu 2p_{3/2} (933 eV). Corrections of binding energy scale for charging effects, for spectra recorded on the GC-supported samples, were done by using the C1s (C-H peak) at 284.8 eV as an internal standard. Spectra were recorded on as-received samples and after sputter-cleaning using argon ion beam of 2 keV for durations of between 180 s and 660 s. The publicly available software XPSPEAK version 4.1,⁵³ was employed for deconvolution of relevant multicomponent spectral regions into appropriate components using mixed Gaussian-Lorentzian functions and Shirley-type baseline subtraction. Appropriate freshly-prepared samples were also subjected to analysis by Inductively Coupled Plasma Mass Spectrophotometry (ICP-MS) in

order to determine their total metal content; the solid deposits were carefully dissolved in ultrahigh-purity aqua regia (3 : 1 HCl / HNO₃ solutions) and suitably diluted with aqueous 1% HCl and 3% HNO₃ solution prior to final ICP-MS analysis.

3. RESULTS AND DISCUSSION

3.1 Current-Potential-Time Variations and Thermodynamic Modelling

Rapid variation in potentials were observed at Stages 3 and 6 in current-potential-time (*i-E-t*) transients recorded during deposition of the nanocluster systems investigated in this work as presented in Figure 2a-c and Figure S1 in the Supporting Information.⁵⁴ The *i-E-t* signals revealed that as soon as open-circuit conditions were set steady open-circuit potential (OCP) values were observed within 40 s, strongly signifying sufficient time for occurrence of SLRR reactions and establishment of interfacial equilibrium conditions. Figure 2d-e presents variations in average OCP during SLRR reactions (averaged over the last 90 s at Stages 3 and 6 as shown in Figure 2a-c). After the second deposition cycle, the OCP during SLRR involving Pt (SLRR_{Pt}) reached a steady value of about +0.7 V (vs Ag/AgCl), approximately +0.9 V (vs SHE), whereas the OCP during SLRR involving Au (SLRR_{Au}) was steady at a value of about +1.0 V (vs Ag/AgCl), approximately +1.2V (vs SHE). The nature of E_{dep} invoked to electrodeposit sacrificial Cu (either UPD or OPD) had an effect only during the first deposition cycle, attributable to different mechanisms of nucleation and growth of metal clusters on the pristine substrate (see Figure 2d-e). Use of OPD Cu resulted in very steady OCP variations during SLRR stages throughout the deposition sequences as shown in Figure 2e - f. The steady nature of the OCP variations observed during SLRR stages strongly indicated some equilibrium situation was established involving solid Pt or Au nanoparticulate surfaces and their corresponding precursor ions and the liberated Cu²⁺ ions as implied by Reactions 2 - 3. Indeed, fast reaction kinetics have been systematically established for SLRR reaction involving Cu UPD and Pt on Au(111)

substrate and the plateau of OCP transients during SLRR step is reflective of equilibrium attainment.⁵⁵

Further insights on expected speciation upon completion of SLRR stages were gained from comparison of OCP to thermochemical E -pH models (Figure 3), computed close to experimental concentrations of aqueous precursors used. Experimentally our main endeavour was utilisation of separate redox reactions between Cu and the noble metals Pt and Au, hence E -pH models were independently optimized for Au-Cu-H₂O or Pt-Cu-H₂O (Figure 3a-b). More appropriately, given that chloride-containing complexed ions were employed as the noble metal precursors, further models were generated for Au-Cu-Cl-H₂O and Pt-Cu-Cl-H₂O systems (Figure 3c-d). In all scenarios, thermodynamic modelling strongly suggested that hydrolysed species and oxides of Cu, namely Cu(OH)₂(s) and Cu₂O_(s), were expected to exist above pH 4 and at potentials greater than about +0.2 V (vs SHE); giving strong support for the use of acidic electrolytes as precursors for SLRR reactions involving Cu. Moreover, the stability of AuCl₄⁻ and PtCl₆²⁻ is clearly revealed in the models inclusive of chloride-containing species (Figure 3c-d): when pH is less than 3 and E greater than 1.2 V (vs SHE), no possibility of the hydrolysed species Au(OH)₃(s) is expected, whereas PtCl₆²⁻ is found to be very stable when pH less than 7 and E greater than 1.1 V (vs SHE). Pt(s) is found to be thermodynamically stable at E less than + 0.9 V (vs SHE) when pH is less than 7. Au(s) is stable at more positive potentials as compared to Pt(s), for instance, at pH less than 3, it is stable when E is less than +1.1 V(vs SHE) (see Figure 3c). The E -pH models revealed that Cu²⁺ is predominant above +0.25 V (vs SHE) when considered with respect to Pt species and predominant above +0.35 V (vs SHE) when considered with respect to Au species.

Comparing the preceding E -pH scenarios to OCP variations during SLRR_{Pt} (Figure 2d-e) – where steady-state OCP of about +0.7 V (vs Ag/AgCl) (or +0.9 V (vs SHE)) was established –

equilibria involving $\text{Pt}^{2+}/\text{Pt(s)}$ and Cu^{2+} were likely to have been responsible for the observed OCP steady-state. Moreover, the above observations indicated that the reduction pathway from PtCl_6^{2-} to Pt(s) during actual SLRR stages (see Reaction 6) might have involved formation of thermodynamically-stable intermediate Pt^{2+} prior to further reduction to Pt(s) and the final equilibrium reached was that between, Cu^{2+} , Pt^{2+} and Pt(s) . Recent work by Gokcen and co-workers⁵⁶ on the issue of stoichiometry of SLRR reaction between PtCl_6^{2-} and Cu(s) indicate that Cu^+ ions may also be involved. From thermodynamic point of view, the inference made was that during reduction of PtCl_6^{2-} the liberated Cl^- ions could have sufficient local concentration on the electrode surface to influence the pathway of Cu adatoms oxidation to Cu(I) instead of Cu(II) ions with probable formation of some CuCl_x^{y-} type of species resulting in apparent stoichiometry of Cu:Pt as 4:1.⁵⁶ On the other hand, the reduction pathway from AuCl_4^- to Au(s) appeared to have proceeded spontaneously as per Reaction 7 as no intermediary Au species were observed in the E -pH models; the OCP during SLRR_{Au} in Figure 2 were very steady at about +1.2 V (vs SHE), the potential at which the species AuCl_4^- and Au(s) share an equilibrium stability boundary at pH 1 (see Figure 3c).

Figure 4 presents variation in total charge (uncorrected for background charge, here assumed not to be significant), determined from integration of current-time (i - t) curves at Stages 2 and 4 during Cu deposition to generate the bimetallic nanoclusters. There is a clear difference for the first cycle when E_{dep} of +0.05 V was employed (see Figure 4a); purely background charge developed as no discernible Cu deposition was expected to occur at the potential concerned. This is in line with OCP observations discussed above as far as the first cycle is concerned. On the other hand, during the first cycle when E_{dep} was -0.05 V, a lesser charge developed indicative of nucleation and growth on pristine glassy carbon surface as compared to subsequent cycles for

which Cu deposition proceeded on either existing Pt or Au nuclei (see Figure 4b). Moreover, with increasing number of cycles a gradual increase of the Cu deposition charge was observed with a tendency to a steady value after the first three cycles, most likely suggestive of a more uniform Cu deposition on the well-developed noble metal clusters. As expected larger values of Cu deposition charge developed when E_{dep} was -0.05 V (Cu OPD) was employed as compared to E_{dep} of $+0.05$ V (Cu UPD) plausibly due to formation of several adlayers of Cu on the growing noble metal clusters as deposition cycles increased when the former E_{dep} was used; submonolayers are typically formed during UPD steps.

All subsequent characterization procedures were performed on the electroodic deposits obtained after eight deposition cycles ($n = 8$) as depicted in Figure 1.

3.2 Microscopic Analysis

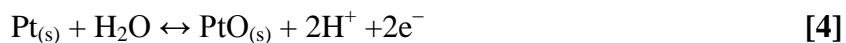
Representative AFM images for the bare GC electrode and the bimetallic $n(\text{Au} | \text{Pt})_{\text{Cu}}/\text{GC}$ system obtained utilising either SLRR reactions involving Cu UPD or Cu OPD and potentiostatic dealloying are shown in Figure 5. AFM revealed reasonably uniform coverage and dispersion on the GC substrate of the deposited nanoclusters consistent with Cu charge variations observed during actual deposition cycles (see Figure 4). Furthermore, AFM revealed – using more detailed 3D images – immobilized needle-like nanocluster morphology (see Figure 5d–e). The observed immobilized clusters varied in height between 5 nm to 40 nm when Cu UPD steps were used and between 10 nm to 80 nm when Cu OPD steps were involved.

The use of Cu UPD as templating adlayers led to much finer nanoclusters which were smaller in their average height and diameter as compared to their counterparts generated utilising OPD steps. This is in line with the fact that multilayers of Cu most likely were generated when OPD steps were used and their subsequent redox-replacement and potentiostatic dealloying led to the morphology observed. On the other hand, the smaller number of adlayers (presumably

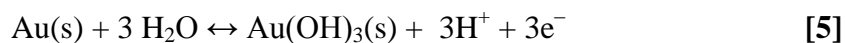
monolayers or submonolayers) had to be replaced when Cu UPD steps were employed. Additional AFM surface plots (Figure 5e–g) clearly revealed growth of closely–neighbourered nanoclusters, reaching almost similar heights and widths, these fused nanoclusters most likely developed due to the close proximity of electrochemically–active sites on which nucleation and growth of metallic nuclei were initiated on the heterogeneous glassy carbon surface. The fact that most of the proximal nanoclusters attained similar heights strongly suggests that their multilayer growth paths during the various deposition cycles were also independent.

3.3. Surface Electrochemistry

Results of cyclic voltammetry (CV) of the as–prepared nanoclusters (recorded in N₂–saturated 0.1 mol/L HClO₄) are presented in Figure 6; the obtained voltammograms depict typical surface electrochemical features of Au and Pt in an acidic environment. CV confirmed that Pt and Au electrochemically–active sites were generated on monometallic nanoclusters (Figure 6; traces *a* and *d*) as well as on the bimetallic nanoclusters (Figure 6; traces *b* and *c*); typical voltammetric features of electroreduction of surface–oxides of Pt (Peak I) and Au (Peak II) in acidic media were observed.⁵⁷⁻⁶⁰ The overall electrochemical processes involving Pt can mainly be attributed to Reaction 4, whose standard reduction potential is 0.980 V (vs SHE), where during anodic scans surface electrooxidation occurred forming PtO(s) films on the nanoclusters and during the cathodic scans electroreduction of the oxide films proceeded to the metallic state Pt(s).



Similarly, electrochemical processes involving Au could primarily be linked to formation of hydrated surface oxides according to Reaction 5, whose standard reduction potential is +1.45 V (vs SHE).



Voltammograms of bimetallic electrodes also exhibited slightly broader reduction peaks (Peaks **I** and **II**; Figure 6) when compared to the monometallic electrodes. This could be attributed to the effect of interfacial interactions between Au and Pt, leading to electronic changes on the Pt and Au electrochemically-active sites and electron-transfer properties. Similar effects have been observed by Obradovic and co-workers on CVs (in N₂-saturated 0.5 mol/L H₂SO₄) of Pt adlayers electrochemically deposited on polycrystalline Au electrodes.⁴³ For the bimetallic clusters, observation of both oxides of Pt and Au reduction peaks strongly indicated that the nanoclusters formed with incomplete top-most layers of a given noble metal, most likely in a multilayered fashion, resulting in presence of electrochemically-active sites of both Au and Pt.

3.4 Surface and Bulk Properties

3.4.1 Electrochemically-Active Surface Area

CV of bare glassy carbon (GC) electrode and those of the various Au and Pt nanostructured electrodes (recorded in 1 mmol/L CuSO₄ and 0.1 mol/L HClO₄ solutions) are presented in Figure S2 (see Supporting Information).⁵⁴ No discernible Cu UPD features were observed on the bare GC but distinguishable bulk Cu deposition from about 0.0 V to -0.2 V and corresponding oxidation (stripping of the bulk deposits) with peak maximum at about +0.08V were clearly observed (Figure S2a) as described in our previous findings.⁴⁵ In all the other cases (Figures S3b-e), which involved monometallic Pt, monometallic Au and their bimetallic counterparts, both deposition as well as stripping of UPD Cu and bulk Cu were observed in the potential range +0.5 V to -0.2 V, whereby during cathodic scans broad Cu UPD features were identifiable in the potential range +0.5 V to +0.05 V in agreement with known electrochemistry of Cu deposition on Pt and Au electrodes.^{51, 61, 62} To further probe the active surfaces of the generated nanocluster electrodes, we utilized ASV involving UPD Cu (see Figure 7). The broad voltammetric features

observed in Figure 7 were indicative of stripping of Cu adlayers from polycrystalline facets of the nanoclusters; on single-crystal surfaces sharp peaks are generally observed.²⁹

The ASV features revealed that the electrochemically synthesized nanoclusters were polycrystalline in nature with various crystallographic facets electrochemically-active. Subsequently, the stripping charges (from integration of the ASV peaks) were used to estimate electrochemically-active surface area (EASA) of the nanoclusters summarised in Table I. The estimated EASA values obtained were about four- to six-fold larger than the geometric area of the bare GC (ca. 0.2 cm²), strongly suggesting that high surface area nanoclusters, with high aspect ratios were generated. The most surface-active electrode was bimetallic $n(\text{Pt} | \text{Au})_{\text{Cu}}/\text{GC}$ followed by $n(\text{Au} | \text{Pt})_{\text{Cu}}/\text{GC}$ and the least active was monometallic $n(\text{Pt})_{\text{Cu}}/\text{GC}$.

3.4.2 ICP-MS Analysis

Results of quantitative analyses of the bulk composition of various Pt-containing nanoclusters, determined using ICP-MS, are summarized in Table I. $n(\text{Au}|\text{Pt})_{\text{Cu}}/\text{GC}$ nanoclusters contained 66 at% Au and 34 at% Pt (or Au : Pt = 2 : 1); whereas the metal distribution in the $n(\text{Pt}|\text{Au})_{\text{Cu}}/\text{GC}$ nanoclusters was 51.5 at% Au and 48.5 at% Pt (or Au : Pt \approx 1 : 1). No detectable traces of Cu in the samples of digested nanoclusters could be found using ICP-MS. The observed metal contents indicated that the nature of the first deposited noble metal had influenced subsequent total metal distribution in the ultimate formed nanoclusters. The interplay of preferential deposition of the more noble Au during sequential codeposition of (Au-Pt) system was clearly revealed metal content was about 80.6 at% Au and 19.4 at % (approximately Au to Pt ratio of 4 : 1). Inspection of the $E-t$ transients during simultaneous SLRR stage involving competition between Pt and Au to replace Cu, there was a significant thermodynamic advantage towards Au deposition over Pt as the overall OCP attained was about +0.9 V (vs Ag/AgCl) or about +1.1 V (vs SHE) (see Figure 1e, Figure 3 and Figure S1c in the Supporting Information).⁵⁴

Clearly, sequential deposition of bimetallic noble metal nanosystems as opposed to sequential codeposition provides a unique set of degrees of freedom in tuning composition of resultant nanostructured deposits.

Using ICP–MS derived metal contents, further normalization of the EASA to account for any effect of total metal loading was carried out (see Table I). Normalization of EASA with respect to Pt content showed that bimetallic $n(\text{Au|Pt})_{\text{Cu}}/\text{GC}$ had slightly higher surface area compared to monometallic $n(\text{Pt})_{\text{Cu}}/\text{GC}$ and the bimetallic $n(\text{Pt|Au})_{\text{Cu}}/\text{GC}$ system had the least surface area. When total metal content (TMC) was used to normalize the EASA, the trend in normalized surface area changed to $n(\text{Pt})_{\text{Cu}}/\text{GC} > n(\text{Au|Pt})_{\text{Cu}}/\text{GC} > n(\text{Pt|Au})_{\text{Cu}}/\text{GC}$.

3.4.3 XPS Analysis

XPS was employed ex-situ to probe surface to near-surface chemical composition of pristine glassy carbon electrode (the substrate in this work) and the Pt-based nanocluster electrodes. XPS is a powerful technique for surface characterization of materials generating chemical information from the outer few atomic layers of the probed material with typical depth range of 10 nm and lateral resolution of about 1 μm .^{63, 64} Samples were probed “as-received” and after sputtering with Ar^+ ions within the XPS chamber. Survey spectra involving extensive binding energy regions are presented in Figure S3 (see Supporting Information).⁵⁴

Qualitative analysis of characteristic photoelectron emission lines revealed that the bare substrate mainly contained carbon and oxygen, whereas the nanocluster systems probed contained carbon, oxygen, platinum, as well as gold (in the case of bimetallic systems). The qualitative XPS results were in line with observations made using surface electrochemistry as well as microscopy providing additional and independent evidence that the nanocluster growth pattern left some exposed carbonaceous spots on the substrate and the surface to near-surface composition of the nanoclusters were of the appropriate noble metals Pt and/or Au.

Figures 8–9 display detailed photoelectron spectra, recorded in relevant binding energy regions related to C 1s, O 1s, Pt 4f, and Au 4f orbitals (additional spectra of as–received and sputter–cleaned samples are presented in Figures S4–S5 in the Supporting Information).⁵⁴ Deconvolution of the C 1s photoelectron spectral curves, using non–linear curve–fitting procedures, revealed at least three spectral components, namely, C–1, C–2, and C–3 in Figure 8a–b and Table II. Curve–fitting with three components resulted in most reasonable full–width–at–half–maximum (FWHM) value of about 1 eV; inclusion of one or two components resulted in much larger values of FWHM. Guided by literature on XPS studies on glassy carbon and related carbonaceous materials and their expected chemical functionalities,^{65, 66} particularly after undergoing electrochemical pretreatment as was done in this work prior to deposition of the nanoclusters, the following assignments were made to the deconvoluted C 1S spectra: (i) C–1 at 284.8 eV was assigned to graphitic carbon (in C–H bonding environment) on the GC surface; (ii) C–2 at about 285.5 eV was assigned to expected phenolic surface functionalities such as –C–OH and –C–NH on the GC surface; and (iii) C–3 (B_E positions in the range 286.3 eV – 286.5 eV) was attributed to carbonyl (–C=O) groups, also mainly from the GC surface and possibly from traces of adventitious adsorbed species.

The O 1s spectra (Figure 8c–d) were found to appropriately fit at least three components with overall FWHM value of 1.5 ± 0.2 eV: (i) O–1 (B_E positions in the range 530.6 – 530.8 eV), (ii) O–2 (B_E positions in the range 531.8 – 532.2 eV), and (iii) O–3 (B_E position about 533 – 533.6 eV). O–1 was mainly attributed to C=O groups on the GC surface and probably some surface metal oxides on the nanoclusters, if they were formed at all. The B_E position of O–2 was typical of C–OH and/or C–O–C groups; O–3 was of the lowest intensity and perhaps was due to chemisorbed oxygen and/or some traces of adsorbed water.⁶⁶ The similarities in XPS binding energy positions of the carbon and oxygen components from the two types of bimetallic systems

strongly indicated that the characteristics of the GC surface did not vary much from one sample to another, appropriately so given the fact that pre- and post-treatment procedures on the GC samples were the same and practically reproducible.

In the case of Pt 4f and Au 4f photoemission spectral regions (see Figure 9a–d) spectral doublets were observed as theoretically expected due to spin-orbit splitting (S.O.S) phenomenon, a consequence of electron spin and angular momentum in the 4f orbitals, $4f_{7/2}$ and $4f_{5/2}$, respectively.^{63, 64} In particular, the Pt 4f spectral regions markedly indicated presence of multiple microstates of Pt as broad peaks with clearly discernible shoulders were observed; compared to the monometallic Pt system the peak features were more distinctly pronounced in the bimetallic systems, suggestive of a strong influence of Au on Pt XPS responses.

Deconvolution of the 4f doublets proceeded by fitting two symmetric mixed Gaussian-Laurentzian functions for every microstate component considered, applying theoretical constraints on the peak area ratios of $4f_{7/2}$ and $4f_{5/2}$ peaks at 4 : 3 with their B_E separations fixed at literature values of 3.30 eV and 3.67 eV for Pt and Au, respectively.⁶⁴ During optimization FWHM of all spectral components ($4f_{7/2}$ and $4f_{5/2}$ peak pairs) considered were set to remain equal. The presence of a single Au $5p_{1/2}$ peak in the same binding energy region of Pt 4f doublets had to be considered in deconvolution of Pt 4f spectral region by inclusion of one additional single peak during fitting procedures on the Pt 4f curves of the bimetallic systems; on XPS of bulk gold systems, the Au $5p_{1/2}$ photoelectron peak occurs at about 74 eV.^{63, 64} Initial attempts to fit the Pt 4f with only two sets of doublets resulted in unreasonably large FWHM values for Pt 4f, such large FWHM values are characteristic of presence of multiple Pt chemical microenvironments.⁶⁷ Three sets of doublets were used in deconvolution of Pt 4f signals in further fitting procedures which resulted in reasonable FWHM values. For consistency the same scenario was employed to fit the Au 4f spectra. Consequently, the Pt 4f and Au 4f spectra were

resolved into three spectral components, namely, Pt-1, Pt-2, Pt-3, Au-1, Au-2, and Au-3 (each component was a doublet composed of $4f_{7/2}$ and $4f_{5/2}$ peaks as depicted in Figure 9).

Detailed Cu 2p XPS region (Figure 9f) did not reveal any analyzable peaks strongly suggesting effective redox-replacement reactions and dealloying steps of the sacrificial Cu used during deposition of the nanocluster systems.

Surface and near-surface content from XPS (that is, concentrations of observed components) were estimated using the relation:

$$C_{\text{At}\%_x} = \frac{\frac{PA_x}{ASF_x}}{\sum \frac{PA_i}{ASF_i}} \times 100 \quad [6]$$

where PA_x , PA_i denote the extracted peak areas of spectral component x or i , respectively; ASF_x , ASF_i denote the atomic sensitivity factors of elemental component x or i (here taken from the relevant literature),⁶⁸ respectively; $C_{\text{At}\%_x}$ denotes the atomic concentration of elemental component x .

Table II summarises the relevant XPS binding energy (B_E) values of deconvoluted Pt and Au $4f_{7/2}$ peaks, overall FWHM values and respective atomic concentrations (for simplicity, B_E values of $4f_{5/2}$ peaks are not shown as they can be deduced from above-mentioned S.O.S considerations). For bulk monometallic Pt systems standard reference literature provide B_E values of the Pt $4f_{7/2}$ peak related to Pt(0) in the range 70.8 – 71.2 eV and oxidized states of Pt have much higher B_E values. For example, B_E values of PtO_x ($x=1,2$) have been reported in the range 73.6 – 75.0 eV and for $\text{Pt}(\text{OH})_2$ in the range 72.4 – 72.8 eV.^{63, 64} In typical nanoparticulate Pt systems, literature reports of the B_E of Pt(0) $4f_{7/2}$ peak are scattered in the range 71.2 – 72.3 eV and oxidized nanoparticulate forms of PtO and PtO_2 have B_E values between 72.6 – 75.6 eV.⁶⁹⁻⁷³ Due to different coordination numbers surface atoms do not behave the same way as bulk atoms

upon their interaction with incident X-ray beams, that is, surface potentials and bulk (or subsurface) potentials are quite distinct. Accordingly, a small shift in core electron binding energy (typically less than 1 eV) of surface atoms relative to bulk atoms can be observed from XPS spectra.⁷⁴ In terms of microstates of monometallic Pt nanoparticles (vapor deposited onto highly oriented pyrolytic graphite (HOPG)), Zhang et al⁷⁰ resolved the Pt 4f XPS signals into three components at B_E values of 71.4 eV, 72.3 eV, and 73.2 eV, respectively, which were attributed to surface Pt(0) atoms, bulk Pt(0) atoms, and surface Pt oxide films (PtO_x) on the nanoparticles, respectively. In light of the above, it is clear that one oxidation state of Pt may generate multiple microstates that can be manifested by observation of multiple peaks in XPS investigations.

Pt spectral components of all nanocluster electrodes investigated in this work exhibited B_E values of Pt 4f_{7/2} peak in the range 70.8 – 72.9 eV (see Table II). Observed B_E values strongly indicated presence of Pt(0), particularly for components Pt–1 and Pt–2. Moreover, Pt–3 could be related to some PtO_x or some Pt–substrate interaction as indicated by aforementioned literature information on Pt XPS characteristics. Furthermore, the B_E values of all the Pt spectral components of the bimetallic nanosystems, $n(\text{Au|Pt})_{\text{Cu}}/\text{GC}$ and $n(\text{Pt|Au})_{\text{Cu}}/\text{GC}$, exhibited a general positive shift of between 0.5 eV and 1 eV when compared to the monometallic Pt system, $n(\text{Pt})_{\text{Cu}}/\text{GC}$. This observation strongly suggested either a significant electronic influence on Pt atoms by incorporation of Au atoms in the nanocluster systems or some nanocluster–substrate interaction.^{69, 71, 72} In particular, the B_E of the Pt–2 component was the greatest at about 1 eV, whereas the corresponding shifts for Pt–1 and Pt–3 components were between 0.5 – 0.7 eV. Most likely Pt–1 was related to surface Pt atoms, Pt–2 was related to Au|Pt interactions in the subsurface of the bimetallic nanoclusters due to its strongest B_E shift when compared to monometallic Pt, and Pt–3 was associated with surface PtO_x and/or metal–substrate interactions

involving surface oxygenated functional groups. Accordingly, the B_E values of the Pt components in the two types of bimetallic systems did not differ much (the values were within 0.1 eV, regardless of the Ar^+ treatment). These observations strongly suggested that the nature of electronic properties of the Pt components in the bimetallic nanoclusters remained essentially the same from one type of nanocluster to the other.

The Au $4f_{7/2}$ B_E values of the spectral components Au-1, Au-2, and Au-3 of the bimetallic nanocluster electrodes ranged from 84.0 to 84.9 eV (see Table II). Typical literature B_E values of Au in zero oxidation state in bulk monometallic Au are in the range of 83.8 – 84.2 eV^{63, 64, 75}; B_E values of Au(0) in nanoparticulate systems have been reported between 83.9 to 84.7 eV, with attribution of more positive B_E values for nanoparticles (when benchmarked to bulk Au) due to nanostructuring effects and/or alloying effects.^{71, 76, 77} Oxidized states of Au generate more positive Au $4f_{7/2}$ B_E values than Au(0), for example, Au(+1) states generate B_E values in the range 85.6 – 85.8 eV, whereas B_E values of Au(+3) range from 86.0 to 86.5 eV.^{75, 77} Therefore, the Au components observed in our work were essentially in the elemental oxidation state. Similar to XPS microstates observed for Pt, the component Au-1 was most likely due to non-interactive surface Au atoms whereas Au-2 and Au-3 components were related to embedded Au atoms with Au|Pt interfacial interactions as well as Au atoms interacting with surface functional groups of the substrate, respectively.

Semi-quantitative XPS analysis (inclusive of C, O, Pt, and Au components) using Equation 6 revealed a general decrease for the oxygen components of both $n(Au|Pt)_{Cu}/GC$ and $n(Pt|Au)_{Cu}/GC$ nanocluster electrodes upon Ar^+ sputtering. In particular, changes in the concentration of components O-2 and O-3 (decrease in both B_E values and content, see Tables II, III and IV), strongly suggested these components were due to adventitious adsorbed oxygenated species, such as H_2O_{ads} , as well as carbonaceous oxygen-containing surface functional groups. In the

$n(\text{Au|Pt})_{\text{Cu}}/\text{GC}$ system an increase of about 10% in total Pt was observed after Ar^+ -sputter treatment, whereas a decrease of about 10% was observed for total Au content. The trend for the Pt and Au contents in the $n(\text{Pt|Au})_{\text{Cu}}/\text{GC}$ system was almost the converse (see Tables III and IV). The preceding observations were consistent with the removal of a thin contamination layer upon Ar^+ sputtering, which subsequently led to availability of more surface-to-near-surface metal content during subsequent measurements. The trends in changes of Pt and Au contents before and after Ar^+ -sputtering were also consistent with multilayer growth pattern of sequentially-deposited nanoclusters which resulted in Au-rich surfaces on the $n(\text{Au|Pt})_{\text{Cu}}/\text{GC}$ nanoclusters as opposed to the Pt-rich surfaces of the $n(\text{Pt|Au})_{\text{Cu}}/\text{GC}$ nanoclusters. The Pt and Au contents obtained from XPS (see Table 4) for the two types of bimetallic nanoclusters somewhat differ from corresponding metal contents derived from ICP-MS (see Table I). This is expectedly the case since ICP-MS essentially probed the metal contents of the entire nanocluster samples whereas XPS probed a few atomic layers of the nanoclusters' surface-to-near surface structures. Overall, ICP-MS and XPS results appropriately showed that the sequence of deposition, the different stoichiometry of SLRR reactions between Pt and Au and the sacrificial Cu (see Reactions 1-3), and potentiostatic dealloying of Cu from layers of either Pt or Au played significant roles in determining the final distribution of Au and Pt in the nanoclusters. It appears, if preferential growth of the nanoclusters was layer-by-layer, then the distribution of the first layer of either Au or Pt, during the first deposition cycle, determined the available sites for the growth of subsequent layers.

Based on B_E values and estimated concentrations of the deconvoluted spectral components from XPS, the following scenarios can aptly describe the surface-to-near surface composition of the nanoclusters as immobilized on glassy carbon: (i) presence of carbon and oxygen surface functional groups from bare areas on the GC surface and their possible interaction with the

nanoclusters, (ii) presence of only zerovalent states of Pt and Au in the nanoclusters, (iii) occurrence of mixed microstates of Pt and Au, due to interfacial interactions between Pt and Au atoms in the bimetallic nanoclusters, and (iv) existence of metal–substrate interactions between first few layers of the nanoclusters where some electronic interplay of exposed Pt and Au surface atoms and oxygenated and carbonaceous surface functional groups of the glassy carbon surface took place. Furthermore, the plausible metal–substrate interactions could be playing a stabilizing role. These deductions are schematically presented in Figure 10.

3.5. Electrocatalysis of Formic Acid Oxidation Reaction (FAOR) and Carbon Monoxide Oxidation

3.5.1 Voltammetric Studies

Electrocatalysis of FAOR (Reaction 11; $E^\circ \approx -0.25$ V (vs SHE))⁷⁸ on the Pt and Au–containing nanostructured electrodes was carried out in 0.5 mol/L HCOOH (in 0.1 mol/L HClO₄) primarily to investigate any differences in the electrocatalytic properties of the nanosystems of interest, as this particular structure–sensitive reaction is technologically and fundamentally very important in applications such as fuel cells. The mechanisms of FAOR electrocatalysis on Pt–based systems are complex and have been a subject of interest for several decades.^{7, 79-81}



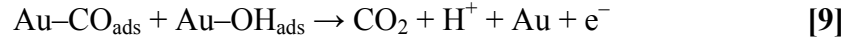
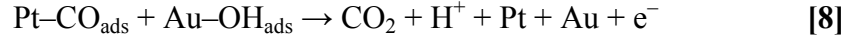
Recent works⁸²⁻⁸⁴ on molecular-level mechanisms of the formic acid oxidation on metal–based catalytic surfaces point out that the reaction should be considered as involving at least three distinct pathways, each commencing from adsorbed HCOOH as schematically shown in Figure 11a. In particular, the direct (or dehydrogenation) pathway to CO₂ likely operates via a weakly-bound reactive HCOOH intermediate and is initiated by C–H bond activation; the indirect (or dehydration) pathway proceeds through strongly–adsorbing intermediates, mainly CO_{ads}, and to a

lesser extent COH_{ads} , and HCO_{ads} ; the formate pathway takes place via a HCOO intermediate and is thought to be initiated by O-H bond activation.⁸²⁻⁸⁴

Figure 11b–c show CV scans of the HCOOH irreversible electrooxidation process on the various nanoclusters that were recorded in gentle flowing solutions at 2mL/min (CV in stationary solutions led to significant bubbles in the cell, in line with formation of CO_2 - Reaction 7 - at high anodic overpotentials). Monometallic Au nanoclusters revealed the lowest current density and exhibited some small activity toward electrooxidation of HCOOH at high overpotentials. Indeed, FAOR on monometallic Au electrodes, investigated by Surface-enhanced Raman Spectroscopy and electrochemistry,⁸⁰ showed that the main reaction occurs via the dehydrogenation pathway with negligible CO_{ads} formation. Monometallic Pt nanoclusters exhibited approximately a ten-fold increase in oxidation peak current density as compared to forward scan oxidation peak of monometallic Au (see Peak I in Figure 11b). The onset of oxidation was also observed at a much more negative potential in the case of monometallic Pt, revealing that these nanoclusters were relatively more electrocatalytically-active than the counterpart monometallic Au nanoclusters toward FAOR. Moreover, the FAOR on monometallic Pt appeared to have proceeded in multiple steps as the broad peak observed in the forward scan (Peak I) was somewhat split into two features (Peak I_a and I_b in Figure 11b), most likely through the indirect and/or formate pathway (see Figure 11a) involving multiple adsorbed intermediates that were oxidized in parallel.^{81, 83} Figure 11c shows CV responses of the HCOOH electrooxidation process on the bimetallic nanoclusters. Compared to the monometallic systems voltammograms recorded on the bimetallic nanoclusters had sharper, more intense peaks suggestive of enhanced overall kinetics of the electrooxidation process; with the $\text{n(Pt|Au)}_{\text{Cu}}/\text{GC}$ exhibiting the highest current densities for the FAOR.

Direct electrooxidation of CO on the nanocluster electrodes was probed by anodic adsorptive stripping voltammetry (Figure 11d); adsorption was carried out in CO-saturated 0.1 mol/L HClO₄ and to eliminate any role of Pt and/or Au oxides formation in the same potential window during CO oxidative stripping the recorded voltammograms were corrected for any background current from independent voltammograms recorded in neat N₂-saturated 0.1 mol/L HClO₄ solutions. In Figure 11d, a very broad, low-intensity voltammogram (peak maximum at about 0.58 V) was observed for the $n(\text{Au})_{\text{Cu}}/\text{GC}$ electrode; the peak was characteristic of diffusion-controlled oxidation voltammograms, indicative of the weak nature of Au to adsorb CO, hence, its oxidation proceeded readily on the monometallic Au sites. On the other hand, a sharp, high intensity stripping peak (peak maximum at 0.63 V) was observed for the $n(\text{Pt})_{\text{Cu}}/\text{GC}$ electrode; the peak is characteristic of CO_{ads} oxidation from monometallic Pt surface.^{43, 85} For bimetallic cases, $n(\text{Pt}|\text{Au})_{\text{Cu}}/\text{GC}$ had its peak maximum at 0.65 V and the maximum for $n(\text{Au}|\text{Pt})_{\text{Cu}}/\text{GC}$ was at about 0.68 V (see Figure 11d). In addition, the stripping peaks exhibited some shoulders at about 0.8 V and 1.15 V, respectively, features that could be attributed to the polycrystalline nature of the nanoclusters which led to adsorption of CO (and its subsequent stripping) from energetically different crystallographic facets. These observations were similar to those of ASV involving Cu UPD (Recall Figure 7). The observed CO electrooxidation suppression on the bimetallic systems relative to monometallic Pt, as evidenced by the drastic change in intensity and shape of the peaks, strongly indicate the influence of Au in the bimetallic systems. Indeed, the positive potential shifts in CO_{ads} stripping peaks of the bimetallic systems relative to monometallic Pt have been observed on AuPt alloy and Pt-decorated Au nanoparticles and attributed to oxidation of CO through Langmuir-Hinshelwood mechanism with strong adsorption of CO.^{85, 86} On the basis of the bifunctional mechanism, DFT studies on the oxidation of adsorbed CO_{ads} indicate that the process may take place through one of the pathways shown in

Reactions 8 to 11, where the oxygen source to form OH_{ads} required is considered to mainly originate from dissociated water on the metallic sites⁸⁷:



DFT calculations on trimers of the type Au₃, Pt₃, Au₂Pt, and AuPt₂ showed that the surface reaction of CO_{ads} with OH_{ads} is energetically more favourable on the alloy trimers than the pure metals.⁸⁷ Further DFT models on CO oxidation on Pt_mAu_n (m + n = 4) clusters by Wang and co-workers¹⁸ indicated that the interaction of CO with Pt in bimetallic clusters is stronger than that with Au. The preceding computational models also revealed that Au atoms play a binary role, that is; to avoid excessive adsorption around the catalytically active Pt centers and to electronically stabilize the active centers.¹⁸

The voltammetric results of Figure 11 strongly suggest that FAOR on the bimetallic nanoclusters investigated in this work proceeded more preferentially through the dehydrogenation pathway than the other FAOR pathways, which appeared to have been favoured on the monometallic Pt nanoclusters. Since in acidic electrolytes, Au is not as effective as Pt in producing surface oxygenated species to facilitate oxidation of CO_{ad}, and therefore the bifunctional effect alone could not be responsible for the enhanced electrocatalytic activity of the bimetallic surfaces in the FAOR,⁴³ ensemble and electronic effects between Au and Pt interfacial sites, uniquely generated in our synthetic protocols, are likely to be at play in promotion of the FAOR on the bimetallic systems. The subtle differences in CO oxidation on the _n(Pt|Au)_{Cu}/GC and _n(Au|Pt)_{Cu}/GC systems most likely arose due to the slight changes in surface-sensitive

synergistic effects on uniquely positioned active sites of the respective nanocluster systems and/or due to their compositional differences as confirmed by XPS and ICP-MS.

3.5.2 Electrochemical Impedance Spectroscopy

Electrochemical Impedance Spectroscopy (EIS)⁸⁸ was deployed to further probe interfacial charge-transfer and adsorptive properties related to the FAOR on the various nanocluster-type electrodes. Impedance responses were obtained in N₂-saturated stationary solutions of 0.5 mol/L HCOOH in 0.1 mol/L HClO₄ at E_{appl} of 0.0 V and 0.1 V, respectively; the potentials were chosen so that the electrooxidation process was expected to proceed with initial adsorption of reactants or intermediates, high degree of kinetic-control and without much perturbation from formation of CO₂ – conditions that ensured high extent of linearity in the EIS measurements.⁸⁸ Modelling of the EIS data was performed through Complex Non-Linear Least-Squares (CNLS) curve-fitting procedures involving equivalent circuits. CNLS fitting using equivalent circuits is used to extract relevant parameters of electrochemical processes with supposition that the electrode and the processes occurring on it behave like typical electrical elements in conventional circuits.⁸⁸ Moreover, it is known that equivalent circuits for electrodic processes with adsorbed species generally should contain at least one capacitor (C) or inductor (L) in addition to the double-layer capacitance (C_{dl}), the charge-transfer resistance (R_{ct}) and solution resistance (R_{s}).⁸⁹

In this work equivalent circuits (Circuits A, B, and C; in Figure 12a) consisted of elements R_{s} , R_{ct} , a constant-phase element (CPE_{dl}) to account for electrode double-layer, pseudo-capacitance related to adsorption (C_{ads}) and the corresponding resistor element associated with any resistance due to adsorptive processes (R_{ads}). Table S1 of the Supporting Information⁵⁴ summarises appropriate mathematical expressions of the total impedance (Z_{T}) and the corresponding real component (Z') and imaginary component (Z'') as functions of frequency (ω) for Circuits A, B, and C. Near-semicircular Nyquist plots and their corresponding fitted curves using Circuits A, B,

and C (that is, complex plots of Z' versus Z'') are shown in Figure 12b–d. Qualitatively, the near-semicircular plots decreased with increasing E_{appl} , indicating less charge–transfer resistance at higher E_{appl} , consistent with accelerated rate of the FAOR at the more positive potential. Furthermore, the $_{\text{n}}(\text{Pt|Au})_{\text{Cu}}/\text{GC}$ electrode exhibited the smallest semicircular Nyquist plots, indicating the least charge–transfer resistance on the nanocluster electrode. The Bode plots, that is, graphical representations of the variation in phase angle (Φ), defined by Equation 12, as a function of the frequency of the EIS perturbation signal are shown in Figure 12e.

$$\Phi = \tan^{-1}\left(\frac{Z''}{Z'}\right) \quad [12]$$

The broad nature of the Bode plots, with amplitudes extending more than one frequency decade were indicative of multiple processes on the nanocluster electrodes with various time constants.⁹⁰ At E_{appl} of 0.0 V the Bode plots of the monometallic $_{\text{n}}(\text{Pt})_{\text{Cu}}/\text{GC}$ and bimetallic $_{\text{n}}(\text{Au|Pt})_{\text{Cu}}/\text{GC}$ systems exhibited almost the same phase angles at the high frequency regions; this was indicative of very similar initial resistive behaviours on the $_{\text{n}}(\text{Pt})_{\text{Cu}}/\text{GC}$ and $_{\text{n}}(\text{Au|Pt})_{\text{Cu}}/\text{GC}$ nanocluster electrodes. Furthermore, the Bode plot for the bimetallic $_{\text{n}}(\text{Pt|Au})_{\text{Cu}}/\text{GC}$ electrode exhibited the narrowest peak, and distinct phase angle response at the high frequency region (negatively shifted as compared to the $_{\text{n}}(\text{Pt})_{\text{Cu}}/\text{GC}$ and $_{\text{n}}(\text{Au|Pt})_{\text{Cu}}/\text{GC}$ systems) – possibly due to the least resistive behaviour and least number of adsorptive species on the $_{\text{n}}(\text{Pt|Au})_{\text{Cu}}/\text{GC}$ electrode. Increasing E_{appl} to 0.1 V led to a general decrease and a shift to higher frequencies in the phase angle maxima, consistent with the increase in the overall reaction rate of the FAOR at more positive applied potentials.

Table S2 in the Supporting Information⁵⁴ summarises extracted parameters from CNLS curve–fitting of EIS spectra of FAOR on the various nanostructured electrodes under consideration. In general, better fits were obtained utilising either Circuit B or C (see Figure 12c–d) – scenarios

which included simulation of adsorptive processes – as compared to fits obtained with Circuit A (Figure 12a) which excluded circuit elements simulating adsorption. These observations strongly suggested that adsorptive processes were occurring in parallel to the charge–transfer processes. In the series of measurements on the various nanocluster electrodes computed R_s values observed were in the range of $4 \Omega - 7 \Omega$ showing that the solution conductivity was excellent and the electrolyte properties had inconsequential variations during various EIS measurements. For both EIS measurements (at 0.0 V and 0.1 V), R_{ct} values decreased in the order $n(\text{Pt|Au})_{\text{Cu}}/\text{GC} > n(\text{Au|Pt})_{\text{Cu}}/\text{GC} > n(\text{Pt})_{\text{Cu}}/\text{GC}$, firmly indicating that the overall reaction rate of the FAOR was highest on the bimetallic electrode $n(\text{Pt|Au})_{\text{Cu}}/\text{GC}$ and lowest on the monometallic $n(\text{Pt})_{\text{Cu}}/\text{GC}$.

In the case of parameters related to CPE_{dl} (see Table S2 in the Supporting Information),⁵⁴ the empirical parameter α was in the range 0.6 – 0.8, due to surface inhomogeneities of the nanocluster electrodes as a result of their characteristic morphologies as was observed above using microscopy.

The average double–layer capacitance (C_{dl}) values were estimated for the various nanocluster electrodes using mathematical relationships involving the constant Q , α , R_s , and R_{ct} detailed in Table S1 of the Supporting Information.⁵⁴ In the cases of monometallic electrode $n(\text{Pt})_{\text{Cu}}/\text{GC}$ and bimetallic $n(\text{Au|Pt})_{\text{Cu}}/\text{GC}$ electrode systems, for both EIS measurements at 0.0 V and 0.1 V, the C_{dl} values, for a given equivalent circuit, were comparable within the range 2.7 – 4.5 μF . On the other hand, the bimetallic system $n(\text{Pt|Au})_{\text{Cu}}/\text{GC}$ markedly exhibited higher C_{dl} values in the range 16 – 25 μF . For all nanocluster electrodes, there was a general decrease in the magnitude of R_{ads} as the perturbation potential increased from 0.0 V to 0.1 V, irrespective of the equivalent circuit used; this trend was consistent with an accelerated reaction at the more positive potential which was probably accompanied by faster rate of removal of adsorbed reactant molecules and

formed intermediate species off the nanocluster surfaces. Furthermore, the lowest R_{ads} values were observed for the $n(\text{Pt|Au})_{\text{Cu}}/\text{GC}$ electrode. Highest C_{ads} values were also obtained for the bimetallic $n(\text{Pt|Au})_{\text{Cu}}/\text{GC}$ electrode as a result to its most electroactive characteristics and unique distribution of surface and near-surface Pt and Au atoms as was that led to it having most pronounced adsorptive properties related to the FAOR.

4. CONCLUSIONS

Multilayered platinum and/or gold-containing nanoclusters (as monometallic or bimetallic systems) were effectively prepared utilizing multistage electrochemical deposition strategies consisting of sequentially-implemented and cyclical steps involving formation of templating Cu adlayers by potentiostatic electrodeposition, surface-limited redox-replacement (an electroless deposition step) of Cu by the nobler metals Pt and/or Au, and final potentiostatic dealloying of remnant Cu. The templating Cu nanoclusters were generated using either UPD or OPD about the equilibrium potential ($E_{\text{Cu}^{2+}/\text{Cu}}$) of the $\text{Cu}^{2+}/\text{Cu}(\text{s})$ redox couple in an acidic medium of 0.1 M HClO_4 (pH 1). Thermodynamic E -pH models and open-circuit potential variations observed experimentally showed that Pt(s) and Au(s) were the main forms expected after Cu SLRR stages where Cu was oxidatively-replaced to Cu^{2+} by PtCl_6^{2-} and AuCl_4^- precursor ions, respectively.

The resulting nanocluster-like multilayered electrodic systems obtained were subjected to various characterizations for their bulk composition, surface area, near-surface atomic distribution topographic and morphological features using microscopic, spectrophotometric, spectroscopic, and electrochemical techniques of AFM, ICP-MS, XPS, CV, ASV, and EIS.

AFM revealed finely-dispersed needle-like nanoclusters where the main topographic difference between nanoclusters generated via underpotentially-deposited and those overpotentially-deposited templating Cu adlayers was in their resultant average heights and diameters in line with Cu deposition charge variations observed during various deposition cycles.

Close proximity of electrochemically-active sites on the glassy carbon surface led to some fused nanoclusters with similar heights and diameters most likely as a consequence of independent multilayer growth paths on the various active sites where nucleation was initiated.

Surface electrochemical studies performed utilising cyclic voltammetry revealed Pt and Au electrochemically-active sites in their monometallic forms and both Pt and Au active sites in the bimetallic nanocluster systems. The most electrochemically-active Pt-based nanocluster electrode system was the bimetallic form $n(\text{Pt|Au})_{\text{Cu}}/\text{GC}$ followed by $n(\text{Au|Pt})_{\text{Cu}}/\text{GC}$ and the least active was the monometallic $n(\text{Pt})_{\text{Cu}}/\text{GC}$; the same trend was established using normalized surface area with respect to total metal contents of the nanocluster systems derived using ICP-MS. Moreover, ICP-MS informed us that sequential codeposition to generate the alloy-type bimetallic system (Au-Pt) led to preferential deposition of the nobler Au, in which case the content of Pt was greatly suppressed.

ASV studies involving Cu UPD on the nanoclusters exhibited typical features of polycrystalline electrodes. Thus, the growth pattern of the nanoclusters whether monometallic or bimetallic resulted in formation of various crystallographic facets which were electrochemically-active.

XPS studies showed typical features of glassy carbon surface functionalities mainly involving multiple forms of carbon and oxygen such as carbonyl and hydroxyl groups and their plausible interactions with the noble metal nanoclusters, effectively stabilizing them. XPS also revealed that the nanoclusters contained zerovalent Pt and Au forms whose surface to near-surface distribution depended on the sequence of their deposition where Pt-rich surface were obtained in the case of $n(\text{Pt|Au})_{\text{Cu}}/\text{GC}$ system and Au-rich ones were generated on the $n(\text{Au|Pt})_{\text{Cu}}/\text{GC}$ system. Furthermore, mixed microstates of Pt and Au were clearly generated in the nanoclusters due to

interfacial bimetallic interactions consistent with multilayer growth pattern of the deposited nanoclusters.

Elaborate electrocatalytic studies performed using CV, ASV, and EIS for the formic acid oxidation reaction and dissolved carbon monoxide adsorption–oxidation process on the nanocluster electrodic systems firmly informed us that the route used to nanostructurally–preorganise bimetallic Au and Pt sites (that is, the order of their deposition) had consequential effects on electrocatalysis. In this regard, the Pt–rich $n(\text{Pt}|\text{Au})_{\text{Cu}}/\text{GC}$ appeared to have superior electrocatalytic activity followed by $n(\text{Au}|\text{Pt})_{\text{Cu}}/\text{GC}$, $n(\text{Pt})_{\text{Cu}}/\text{GC}$ and $n(\text{Au})_{\text{Cu}}/\text{GC}$ as the least active systems. The direct (or dehydrogenation) pathway of FAOR was likely predominant on the bimetallic systems and the indirect or formate pathways most likely occurred preferentially on the monometallic Pt systems.

Sequential electrochemical synthetic strategies employed here clearly exhibited their unique advantage as opposed to methods involving codeposition. Moreover, the inherent feature of sequential generation of multilayered nanoclusters is in tuning electrocatalysis of bimetallic systems such as those involving Pt and Au.

ACKNOWLEDGEMENTS

Funding and provision of research facilities from University of Pretoria and CSIR are greatly appreciated. The authors also wish to acknowledge Prof. W. D. Roos, C. Jafta, T. Malwela, and Dr. T. Hillie of the Department of Physics, University of the Free State and MSM Unit, CSIR, respectively, for their technical assistances in regard to XPS and AFM. T. S. M thanks the CSIR for a doctorate studentship.

SUPPORTING INFORMATION

Figures S1 – S5 and Tables S1 and S2 containing supporting information on: (i) Additional potential–time ($E-t$) transients; (ii) cyclic voltammetry of Cu electrodeposition on bare glassy carbon and on various nanocluster electrodes; (iii) X–ray photoelectron spectra of bare glassy carbon and various nanocluster electrodes; (iv) mathematical expressions of impedances of various equivalent circuits used in modelling charge–transfer and adsorptive aspects using electrochemical impedance spectroscopy.

APPENDIX A: Nomenclature

$M N$	Bimetallic system consisting of adlayers of metals N and M , deposited separately (a stack of metallic N and M adlayers)
$SLRR_M$	Surface–limited redox–replacement of a sacrificial metal, e.g. Cu, by more noble metal M (e.g. $M = Pt$ or Au) from a single noble metal precursor solution.
${}_n(Pt)_{Cu}/GC$	Glassy carbon supported n –layered monometallic Pt nanostructure obtained through n cycles of sequential open circuit surface–limited redox– replacement of a sacrificial Cu adlayers by metallic Pt from its precursor salt.
${}_n(Au)_{Cu}/GC$	Glassy carbon supported n –layered monometallic Au nanostructure obtained through n cycles of sequential open circuit surface–limited redox –replacement of a sacrificial Cu adlayers by metallic Au from its precursor salt.
${}_n(Au Pt)_{Cu}/GC$	Glassy carbon supported n –layered nanostructure obtained through n cycles of (i) sequential open circuit surface–limited redox–replacement of

sacrificial Cu adlayers by Pt from a Pt salt solution, followed by (ii) sequential open circuit surface-limited redox-replacement of sacrificial Cu adlayers by Au from a Au salt solution. The first and last layer in this system is made of Pt and Au, respectively.

$n(\text{Pt|Au})_{\text{Cu}}/\text{GC}$

Glassy carbon supported n -layered nanostructure obtained through n cycles of (i) sequential open circuit surface-limited redox-replacement of sacrificial Cu adlayers by Au from a Au salt solution, followed by (ii) sequential open circuit surface-limited redox-replacement of sacrificial Cu adlayers by Pt from a Pt salt solution. The first and last layer in this system is made of Au and Pt, respectively.

$n(\text{Au-Pt})_{\text{Cu}}/\text{GC}$

Glassy carbon supported n -layered nanostructure obtained through n cycles, each involving sequential open circuit surface-limited redox-replacement of sacrificial Cu adlayers by Pt and Au from a mixed precursor solution to form alloy-type bimetallic layers.

REFERENCES

1. M. Watanabe, in *Catalysis and Electrocatalysis at Nanoparticle Surfaces*, A. Wieckowski, E. R. Savinova and C. G. Vayenas, Editors, p. 827, CRC Press, Boca Raton (2003).
2. N. R. Shiju and V. V. Guliants, *Appl. Catal., A*, **356**, 1 (2009).
3. F. Raimondi, G. G. Scherer, R. Kötz and A. Wokaun, *Angew. Chem. Int. Ed.*, **44**, 2190 (2005).
4. R. Ferrando, J. Jellinek and R. L. Johnston, *Chem. Rev.*, **108**, 845 (2008).
5. J. D. Aiken III and R. G. Finke, *J. Mol. Cat. A*, **145**, 1 (1999).
6. A. Chen and P. Holt-Hindle, *Chem. Rev.*, **110**, 3767 (2010).
7. R. Adzic, in *Encyclopedia of Electrochemistry*, A. J. Bard, M. Stratmann, E. Gileadi and M. Urbakh, Editors, Vol. 1, p. 561, WILEY-VCH, Weinheim (2002).
8. R. Parsons and T. VanderNoot, *J. Electroanal. Chem.*, **257**, 9 (1988).
9. F. Maroun, F. Ozanam, O. M. Magnussen and R. J. Behm, *Science*, **293**, 1811 (2001).
10. P. N. Ross, in *Electrocatalysis*, J. Lipkowski and P. N. Ross, Editors, p. 43, Wiley, New York (1998).
11. E. Antolini, *J. Power Sources*, **170**, 1 (2007).
12. O. A. Petrii, *J. Solid State Electrochem.*, **12**, 609 (2008).
13. M. F. Mrozek, H. Luo and M. J. Weaver, *Langmuir*, **16**, 8463 (2000).

14. B. Hammer and J. K. Norskov, *Nature*, **376**, 238 (1995).
15. J. K. Norskov, T. Bligaard, J. Rossmeisl and C. H. Christensen, *Nature Chemistry*, **1**, 37 (2009).
16. J. Zhang, K. Sasaki, E. Sutter and R. R. Adzic, *Science*, **315**, 220 (2007).
17. C. Song, Q. Ge and L. Wang, *J. Phys. Chem. B*, **109**, 22341 (2005).
18. F. Wang, D. Zhang and Y. Ding, *J. Phys. Chem. C*, **114**, 14076 (2010).
19. K. A. Friedrich, K. P. Geyzers, A. J. Dickinson and U. Stimming, *J. Electroanal. Chem.*, **524-525**, 261 (2002).
20. S. Litster and G. McLean, *J. Power Sources*, **130**, 61 (2004).
21. S. D. Thompson, L. R. Jordan and M. Forsyth, *Electrochimica Acta*, **46**, 1657 (2001).
22. S. Ye and K. Uosaki, in *Encyclopedia of Electrochemistry*, A.J. Bard and M. Stratman, Editors, Vol. 1, p. 471, Wiley-VCH, Weinheim (2002).
23. S. Chen and A. Kucernak, *J. Phys. Chem. B*, **107**, 8392 (2003).
24. C. R. K. Rao and D. C. Trivedi, *Coord. Chem. Rev.*, **249**, 613 (2005).
25. J. V. Zoval, J. Lee, S. Gorer and R. M. Penner, *J. Phys. Chem. B*, **102**, 1166 (1998).
26. L. M. Plyasova, I. Y. Molina, A. N. Gavrilov, S. V. Cherepanova, O. V. Cherstiouk, N. A. Rudina, E. R. Savinova and G. A. Tsirlina, *Electrochim. Acta*, **51**, 4477 (2006).
27. G. Lu and G. Zangari, *J. Phys. Chem. B*, **109**, 7998 (2005).

28. C. Coutanceau, S. Brimaud, C. Lamy, J.-M. Leger, L. Dubau, S. Rousseau and F. Vigier, *Electrochem. Acta*, **53**, 6865 (2008).
29. E. Herrero, L. J. Buller and H. D. Abruna, *Chem. Rev.*, **101**, 1897 (2001).
30. M. Paunovic and M. Schlesinger, *Fundamentals of Electrochemical Deposition*, 2nd ed., p. 139, John Wiley & Sons, New Jersey (2006).
31. W. Chrzanowski and A. Wieckowski, *Langmuir*, **13**, 5974 (1997).
32. S. S. Djokić and P. L. Cavallotti, in *Modern Aspects of Electrochemistry*, S. S. Djokić, Editor, Vol. 48, p. 251 Springer Science+Business Media, LLC, New York (2010).
33. S. R. Brankovic, J. X. Wang and R. R. Adzic, *Surf. Sci.*, **474**, L173 (2001).
34. Y.-G. Kim, J. Y. Kim, D. Vairavapandian and J. L. Stickney, *J. Phys. Chem. B*, **110**, 17998 (2006).
35. C. Thambidurai, Y. Kim and J. L. Stickney, *Electrochim. Acta*, **53**, 6157 (2008).
36. M. F. Mrozek, Y. Xie and M. J. Weaver, *Anal. Chem.*, **73**, 5953 (2001).
37. R. E. Rettew, J. W. Guthrie and F. M. Alamgir, *J. Electrochem. Soc.*, **156**, D513 (2009).
38. P. Strasser, *Rev. Chem. Eng.*, **25**, 255 (2009).
39. P. Strasser, S. Koh and J. Greeley, *Phys. Chem. Chem. Phys.*, **10**, 3670 (2008).
40. S. Cherevko, N. Kulyk and C.-H. Chung, *Langmuir*, **28**, 3306 (2012).

41. C. Xu, Y. Liu, J. Wang, H. Geng and H. Qiu, *ACS Appl. Mater. Interfaces*, **3**, 4626 (2011).
42. M. Mohl, A. Kumar, A. L. m. Reddy, A. Kukovecz, Z. Konya, I. Kiricsi, R. Vajtai and P. M. Ajayan, *J. Phys. Chem. C*, **114**, 389 (2010).
43. M. D. Obradovic, A. V. Tripkovic and S. L. Gojkovic, *Electrochim. Acta*, **55**, 204 (2009).
44. T. S. Mkwizu, M. K. Mathe and I. Cukrowski, *ECS Trans.*, **19**, 97 (2009).
45. T. S. Mkwizu, M. K. Mathe and I. Cukrowski, *Langmuir*, **26**, 570 (2010).
46. J. F. Rivadulla, M. C. Vergara, M. C. Blanco, M. A. Lopez-Quintela and J. Rivas, *J. Phys. Chem. B*, **101**, 8997 (1997).
47. A. Usher, D. C. McPhail and J. Brugger, *Geochim. Cosmochim. Acta* **73**, 3359 (2009).
48. F. A. Cotton and G. Wilkinson, *Advanced Inorganic Chemistry*, 5th ed., p. 776, John Wiley & Sons, Toronto (1988).
49. C. W. Bale, P. Chartrand, S. A. Degterov, G. Eriksson, K. Hack, R. Ben Mahfoud, J. Melançon, A. D. Pelton and S. Petersen, *Calphad*, **26**, 189 (2002).
50. B. A. Boukamp, *Solid State Ionics*, **20**, 31 (1986).
51. C. L. Green and A. Kucernak, *J. Phys. Chem. B*, **106**, 1036 (2002).
52. C. L. Green and A. Kucernak, *J. Phys. Chem. B*, **106**, 11446 (2002).

53. R. W. M. Kwok, *XPSPEAK, 4.1*, The Chinese University of Hong Kong, Shatin, Hong Kong (2000).
54. See Supporting Information available at <http://dx.doi.org/>
55. D. Gokcen, S.-E. Bae and S. R. Brankovic, *Electrochim. Acta*, **56**, 5545 (2011).
56. D. Gokcen, S.-E. Bae and S. R. Brankovic, *J. Electrochem. Soc.*, **157**, D582 (2010).
57. S. Trasatti and O. A. Petrii, *J. Electroanal. Chem.*, **327**, 353 (1992).
58. A. Bard and L. R. Faulkner, *Electrochemical methods: Fundamentals and Applications*, 2nd ed., p. 570, John-Wiley & Sons, New York (2001).
59. L. D. Burke and P. F. Nugent, *Gold Bulletin*, **30**, 43 (1997).
60. G. Jerkiewicz, G. Vantkhah, J. Lessard, M. P. Soriaga and Y.-S. Park, *Electrochim. Acta*, **49**, 1451 (2004).
61. J. G. Xu and X. W. Wang, *Surf. Sci.*, **408**, 317 (1998).
62. M. R. Deakin and O. Melroy, *J. Electroanal. Chem.*, **239**, 321 (1988).
63. D. Briggs and M. P. Seah, *Practical Surface Analysis*, 2nd ed., Vol. 1, p. John Wiley & Sons, New York (1993).
64. J. F. Moulder, W. F. Stickle, P. E. Sobol and K. D. Bomben, *Handbook of X-ray Photoelectron Spectroscopy*, Physical Electronics, Inc., Eden Prairie (1995).
65. A. Dekanski, J. Stevanović, R. Stevanović and B. Ž. Nikolić, *Carbon*, **39**, 1195 (2001).

66. Z. R. Yue, W. Jiang, L. Wang, S. D. Gardner and C. U. Pittman Jr, *Carbon*, **37**, 1785 (1999).
67. S. Manandhar and J. A. Kelber, *Electrochim. Acta*, **52**, 5010 (2007).
68. J. H. Scofield, *J. Electron Spectrosc. Relat. Phenom.*, **8**, 129 (1976).
69. F. Şen and G. Gökağaç, *J. Phys. Chem. C*, **111**, 5715 (2007).
70. G. Zhang, D. Yang and E. Sacher, *J. Phys. Chem. C*, **111**, 565 (2007).
71. J. R. Croy, S. Mostafa, L. Hickman, H. Heinrich and B. R. Cuenya, *Appl. Catal., A*, **350**, 207 (2008).
72. Y. Zhang, Q. Huang, Z. Zou, J. Yang, W. Vogel and H. Yang, *J. Phys. Chem. C*, **114**, 6860 (2010).
73. S. Kim, C. Jung, J. Kim, C. K. Rhee, S. Choi and T. Lim, *Langmuir*, **26**, 4497 (2010).
74. S. E. Hörnström and L. Johansson, *Surf. Sci.*, **160**, 561 (1985).
75. M. Peuckert, F. P. Coenen and H. P. Bonzel, *Surf. Sci.*, **141**, 515 (1984).
76. C. Berg, H. J. Venvik, F. Strisland, A. Ramstad and A. Borg, *Surf. Sci.*, **409**, 1 (1998).
77. M. P. Casalotto, A. Longo, A. Martorana, A. Prestianni and A. M. Venezia, *Surf. Interface Anal.*, **38**, 215 (2006).
78. X. Yu and P. G. Pickup, *J. Power Sources*, **182**, 124 (2008).
79. A. Capon and R. Parsons, *Electroanal. Chem. Interfacial Electrochem.*, **44**, 1 (1973).

80. M. F. Mrozek, H. Luo and M. J. Weaver, *Langmuir*, **16**, 8463 (2000).
81. S. Uhm, H. J. Lee and J. Lee, *Phys. Chem. Chem. Phys.*, **11**, 9326 (2009).
82. A. Cuesta, G. Cabello, M. Osawa and C. Gutiérrez, *ACS Catal.*, **2**, 728 (2012).
83. W. Gao, J. A. Keith, J. Anton and T. Jacob, *J. Am. Chem. Soc.*, **132**, 18377 (2010).
84. Y.-X. Chen, M. Heinen, Z. Jusys and R. J. Behm, *Langmuir*, **22**, 10399 (2006).
85. G. Chen, Y. Li, D. Wang, L. Zheng, G. You, C.-J. Zhong, L. Yang and F. Cai, *J. Power Sources*, **196**, 8323 (2011).
86. F. J. E. Scheijen, G. L. Beltramo, S. Hoepfener, T. H. M. Housmans and M. T. M. Koper, *J. Solid State Electrochem.*, **12**, 483 (2008).
87. J. Zhang, H. Ma, D. Zhang, P. Liu, F. Tian and Y. Ding, *Phys. Chem. Chem. Phys.*, **10**, 3250 (2008).
88. A. Lasia, in *Modern Aspects of Electrochemistry*, B. E. Conway, J. Bockris and R. E. White, Editors, Vol. 32, p. 143, Kluwer Academic/Plenum Publishers, New York (1999).
89. D. A. Harrington and P. Van den Driessche, *J. Electroanal. Chem.*, **501**, 222 (2001).
90. A. L. Ocampo, M. Miranda-Hernandez, J. Morgado, J. A. Montoya and P. J. Sebastian, *J. Power Sources*, **160**, 915 (2006).

Table I. Metal contents and corresponding electrochemically–active surface area (EASA) of various Pt–based nanoclusters

Electrode System	Metal Content ^a		EASA ^b (cm ²)	Normalized	Normalized
	(At. %)			EASA ^c (cm ² /g _{Pt})	EASA ^d (cm ² /g _{TMC})
	<i>Pt</i>	<i>Au</i>			
_n (Pt) _{Cu} /GC	100	–	0.77	1.65 × 10 ⁵	1.65 × 10 ⁵
_n (Au Pt) _{Cu} /GC	34.0	66.0	0.82	1.69 × 10 ⁵	5.70 × 10 ⁴
_n (Pt Au) _{Cu} /GC	48.5	51.5	0.71	7.17 × 10 ⁴	3.46 × 10 ⁴
_n (Au–Pt) _{Cu} /GC	19.4	80.6	–	–	–

^a Determined by ICP–MS; ^b Obtained using anodic stripping voltammetry involving Cu UPD;

^c With respect to Pt content; ^d With respect to Total Metal Content (TMC).

Table II. Binding energy values of deconvoluted X-ray photoelectron spectral components of the Pt-containing nanoclusters

Electrode System	Binding Energy, B_E / eV											
	C 1s			O 1s			Pt 4f _{7/2}			Au 4f _{7/2}		
	C-1	C-2	C-3	O-1	O-2	O-3	Pt-1	Pt-2	Pt-3	Au-1	Au-2	Au-3
$n(\text{Pt})_{\text{Cu}}/\text{GC}^a$	284.8	285.4	286.5	–	–	–	70.8	71.0	72.2	–	–	–
	<i>(FWHM = 1.2 eV)</i>			–			<i>(FWHM = 1.2 eV)</i>			–		
$n(\text{Au Pt})_{\text{Cu}}/\text{GC}^a$	284.8	285.5	286.4	530.6	532.2	533.5	71.3	72.1	72.6	84.0	84.4	84.7
	<i>(FWHM = 1.0 eV)</i>			<i>(FWHM = 1.6 eV)</i>			<i>(FWHM = 1.2 eV)</i>			<i>(FWHM = 0.8 eV)</i>		
$n(\text{Au Pt})_{\text{Cu}}/\text{GC}^s$	284.8	285.1	286.5	530.8	532.0	533.0	71.2	72.2	72.7	84.3	84.6	84.9
	<i>(FWHM = 1.2 eV)</i>			<i>(FWHM = 1.4 eV)</i>			<i>(FWHM = 1.1 eV)</i>			<i>(FWHM = 0.8 eV)</i>		
$n(\text{Pt Au})_{\text{Cu}}/\text{GC}^a$	284.8	285.5	286.5	530.7	532.3	533.6	71.3	72.2	72.9	84.1	84.4	84.8
	<i>(FWHM = 1.1 eV)</i>			<i>(FWHM = 1.4 eV)</i>			<i>(FWHM = 1.2 eV)</i>			<i>(FWHM = 1.0 eV)</i>		
$n(\text{Pt Au})_{\text{Cu}}/\text{GC}^s$	284.8	285.5	286.3	530.8	531.8	532.9	71.3	72.3	72.8	84.2	84.5	84.9
	<i>(FWHM = 1.1 eV)</i>			<i>(FWHM = 1.3)</i>			<i>(FWHM = 1.1 eV)</i>			<i>(FWHM = 0.9 eV)</i>		

^a As-received sample; ^s Sample sputtered with Ar⁺

Table III. Surface and near-surface composition of the bimetallic nanocluster electrodes as determined from XPS semi-quantitative analysis involving carbon, oxygen, platinum, and gold spectral components

Electrode System	Content ^b (At %)											
	C			O			Pt			Au		
	C-1	C-2	C-3	O-1	O-2	O-3	Pt-1	Pt-2	Pt-3	Au-1	Au-2	Au-3
$n(\text{Au Pt})_{\text{Cu}}/\text{GC}^a$	19.9%	20.1%	5.8%	10.8%	10.8%	5.9%	2.2%	1.4%	1.4%	7.5%	9.7%	4.8%
	<i>(Total C = 45.8%)</i>			<i>(Total O = 27.3%)</i>			<i>(Total Pt = 4.9%)</i>			<i>(Total Au = 22.0%)</i>		
$n(\text{Au Pt})_{\text{Cu}}/\text{GC}^s$	19.3%	18.9%	8.5%	9.3%	4.1%	2.4%	5.7%	3.1%	1.9%	9.2%	12.0%	5.8%
	<i>(Total C = 46.8%)</i>			<i>(Total O = 15.8%)</i>			<i>(Total Pt = 10.4%)</i>			<i>(Total Au = 27.0%)</i>		
$n(\text{Pt Au})_{\text{Cu}}/\text{GC}^a$	22.0%	18.9%	4.9%	7.8%	6.9%	4.0%	6.5%	3.6%	1.2%	9.9%	11.4%	3.0%
	<i>(Total C = 45.8%)</i>			<i>(Total O = 18.7%)</i>			<i>(Total Pt = 11.3%)</i>			<i>(Total Au = 24.2%)</i>		
$n(\text{Pt Au})_{\text{Cu}}/\text{GC}^s$	14.2%	14.4%	6.2%	6.5%	3.0%	2.2%	7.1%	3.1%	1.4%	13.1%	22.7%	6.3%
	<i>(Total C = 34.7%)</i>			<i>(Total O = 11.6%)</i>			<i>(Total Pt = 11.6%)</i>			<i>(Total Au = 42.5%)</i>		

^a As received; ^b Content estimation inclusive of C, O, Pt, and Au; ^s Sample sputtered with Ar⁺

Table IV. Surface and near-surface composition of Pt-containing nanoclusters electrodes as determined from XPS semi-quantitative analysis involving platinum and gold spectral components

Electrode System	Content ^b / At %					
	Pt			Au		
	Pt-1	Pt-2	Pt-3	Au-1	Au-2	Au-3
$n(\text{Pt})_{\text{Cu}}/\text{GC}^a$	36.1%	48.2%	15.7%	–	–	–
	<i>(Total Pt = 100%)</i>				–	
$n(\text{Au} \text{Pt})_{\text{Cu}}/\text{GC}^a$	8.0%	5.1%	5.0%	27.9%	36.2%	17.7%
	<i>(Total Pt = 18.2%)</i>				<i>(Total Au = 81.8%)</i>	
				<i>(Pt : Au = 1.0 : 4.5)</i>		
$n(\text{Au} \text{Pt})_{\text{Cu}}/\text{GC}^s$	15.2%	8.4%	4.2%	24.6%	32.0%	15.6%
	<i>(Total Pt = 27.8%)</i>				<i>(Total Au = 72.2%)</i>	
				<i>(Pt : Au = 1.0 : 2.6)</i>		
$n(\text{Pt} \text{Au})_{\text{Cu}}/\text{GC}^a$	18.3%	10.1%	3.4%	27.9%	32.0%	8.4%
	<i>(Total Pt = 31.8%)</i>				<i>(Total Au = 68.2%)</i>	
				<i>(Pt : Au = 1.0 : 2.1)</i>		
$n(\text{Pt} \text{Au})_{\text{Cu}}/\text{GC}^s$	13.3%	5.8%	2.5%	24.3%	42.3%	11.8%
	<i>(Total Pt = 21.6%)</i>				<i>(Total Au = 78.4%)</i>	
				<i>(Pt : Au = 1.0 : 3.6)</i>		

^a As received; ^b Content estimation inclusive of Pt and Au only; ^s Sample sputtered with Ar⁺

FIGURE CAPTIONS

Figure 1. Schemes showing electrochemical deposition strategies explored to generate immobilized (a) – (b) bimetallic nanoclusters involving Au and Pt from separate precursors; (c) monometallic Pt or Au nanoclusters, and (d) codeposited bimetallic nanoclusters involving Au and Pt from mixed precursors.

Figure 2. (Color Online) Current–potential–time (i – E – t) transients recorded during deposition of the bimetallic nanoclusters: (a) $n(\text{Au|Pt})_{\text{Cu}}/\text{GC}$, utilising Cu UPD steps, (b) $n(\text{Au|Pt})_{\text{Cu}}/\text{GC}$ involving Cu OPD steps, and (c) $n(\text{Pt|Au})_{\text{Cu}}/\text{GC}$, where Cu OPD steps were employed. (d) – (f) Variations in average open–circuit potential (OCP) during the final 90 s of SLRR stages.

Figure 3. Thermochemical E –pH models for (a) Au–Cu–H₂O, (b) Pt–Cu–H₂O, (c) Au–Cu–Cl–H₂O and (d) Pt–Cu–Cl–H₂O systems at 298.15 K and molality for all aqueous forms of Pt, Au and Cu considered in the model set at 1×10^{-3} mol/Kg.

Figure 4. (Color Online) Variation in total charge developed during Cu deposition stages prior to redox–replacement reactions to generate bimetallic nanoclusters (a) $n(\text{Au|Pt})_{\text{Cu}}/\text{GC}$ using UPD Cu at +0.05 V, (b) $n(\text{Au|Pt})_{\text{Cu}}/\text{GC}$ nanoclusters using OPD Cu at –0.05 V, and (c) $n(\text{Pt|Au})_{\text{Cu}}/\text{GC}$ using OPD Cu at +0.05 V.

Figure 5. (Color Online) Tapping mode AFM images of glassy carbon surface after deposition of Au|Pt bimetallic nanoclusters obtained after eight deposition cycles. (a) A $1 \mu\text{m} \times 4 \mu\text{m}$ top-viewed area of the bare GC; (b) A $4 \mu\text{m} \times 4 \mu\text{m}$ top-viewed area of nanoclusters generated via Cu UPD steps; (c) A $4 \mu\text{m} \times 4 \mu\text{m}$ top-viewed area of nanoclusters generated via Cu OPD steps; (d) A $4 \mu\text{m} \times 4 \mu\text{m}$ surface plot corresponding to (b); (e) A $4 \mu\text{m} \times 4 \mu\text{m}$ surface plot

corresponding to (c); (f) A 2 μm x 2 μm surface plot corresponding to (b). (g) A 2 μm x 2 μm surface plot corresponding to (c).

Figure 6. Cyclic voltammograms of the as-prepared monometallic and bimetallic nanoclusters recorded in N_2 -saturated 0.1 mol/L HClO_4 electrolyte. In all cases the scan rate was 50 mV/s and 5th cycles were taken for this analysis.

Figure 7. Anodic stripping voltammograms after Cu UPD at + 0.05 V for 90s on various Pt and Au nanoclusters recorded from N_2 -saturated 1 mmol/L CuSO_4 in 0.1 mol/L HClO_4 . In all cases, the scans were performed in the direction indicated by broken arrows at 50 mV/s. Background current correction was done by subtraction of voltammograms recorded in neat 0.1M HClO_4 .

Figure 8. (Color Online) X-ray photoelectron spectra (points) and their corresponding deconvoluted spectral components (solid lines) of various bimetallic nanoclusters. Spectra correspond to photoelectrons from (a) – (b) C 1S; and (c) – (d) O 1S orbitals. Probed samples were sputtered with Argon ions.

Figure 9. (Color Online) X-ray photoelectron spectra (points) and their corresponding deconvoluted spectral components (solid lines) recorded from as-received samples of mono- and bimetallic nanoclusters, in the binding energy regions corresponding to photoelectrons ordinarily from (a) – (c) Pt 4f, (d) – (e) Au 4f and (f) Cu 2p orbitals.

Figure 10. (Color Online) Schematic drawings of sequentially deposited multilayered bimetallic nanoclusters of platinum and gold with glassy carbon as the substrate.

Figure 11. (Color Online) (a) Scheme showing plausible mechanistic aspects of formic acid electrooxidation. (b)–(c) Cyclic voltammograms related to formic acid oxidation reaction

(FAOR) on monometallic and bimetallic nanoclusters of Pt and Au; scans were carried out in N₂-saturated 0.5 mol/L HCOOH (in 0.1 mol/L HClO₄) in the anodic direction to +1 V (as indicated by the dotted arrows), followed by cathodic direction; 5th cycles were taken for this analysis. (d) Linear sweep voltammograms of CO electrooxidation after CO-saturation in 0.1 mol/L HClO₄ on the monometallic and bimetallic systems. In all cases, the scan rate was 50 mV/s and $n = 8$.

Figure 12. (a) Equivalent circuits used for modelling electrochemical impedance responses of the Pt-based electrocatalysts. (b) – (d) Complex plane impedance plots (Nyquist plots) fitted using (b) Circuit A, (c) Circuit B, and (d) Circuit C; points are experimental data and solid lines correspond to fitted curves. (e) Bode plots of impedance responses. All measurements were performed from N₂-saturated 0.5 mol/L HCOOH (in 0.1 mol/L HClO₄) solutions.

FIGURE 1

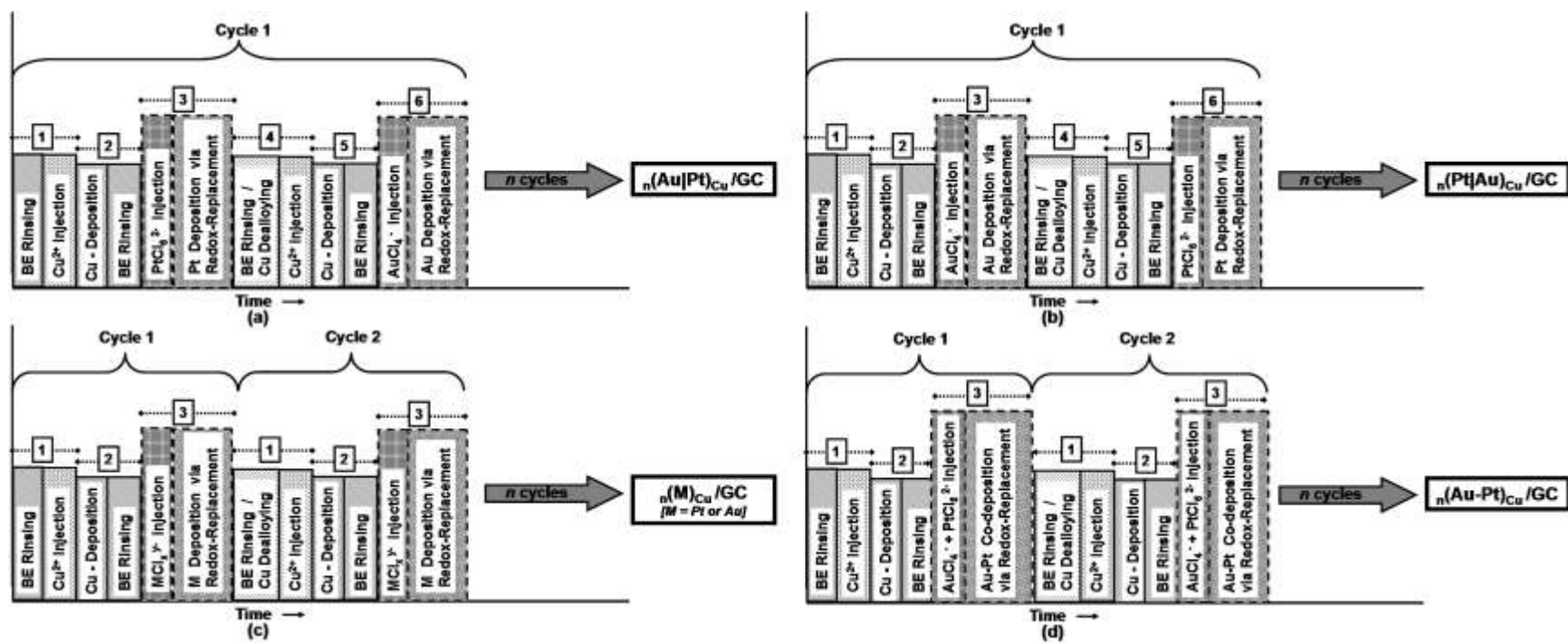


FIGURE 2

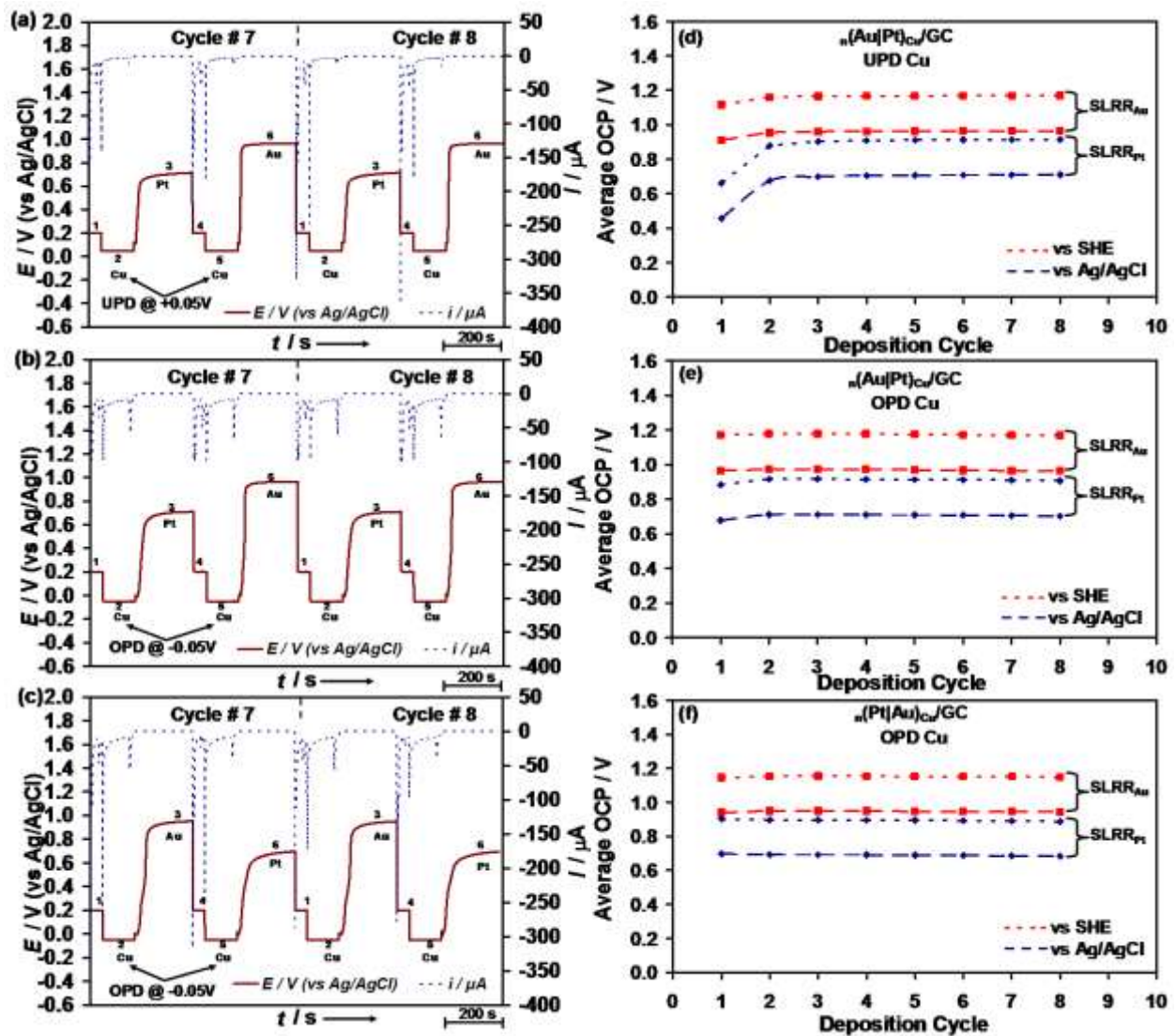


FIGURE 3

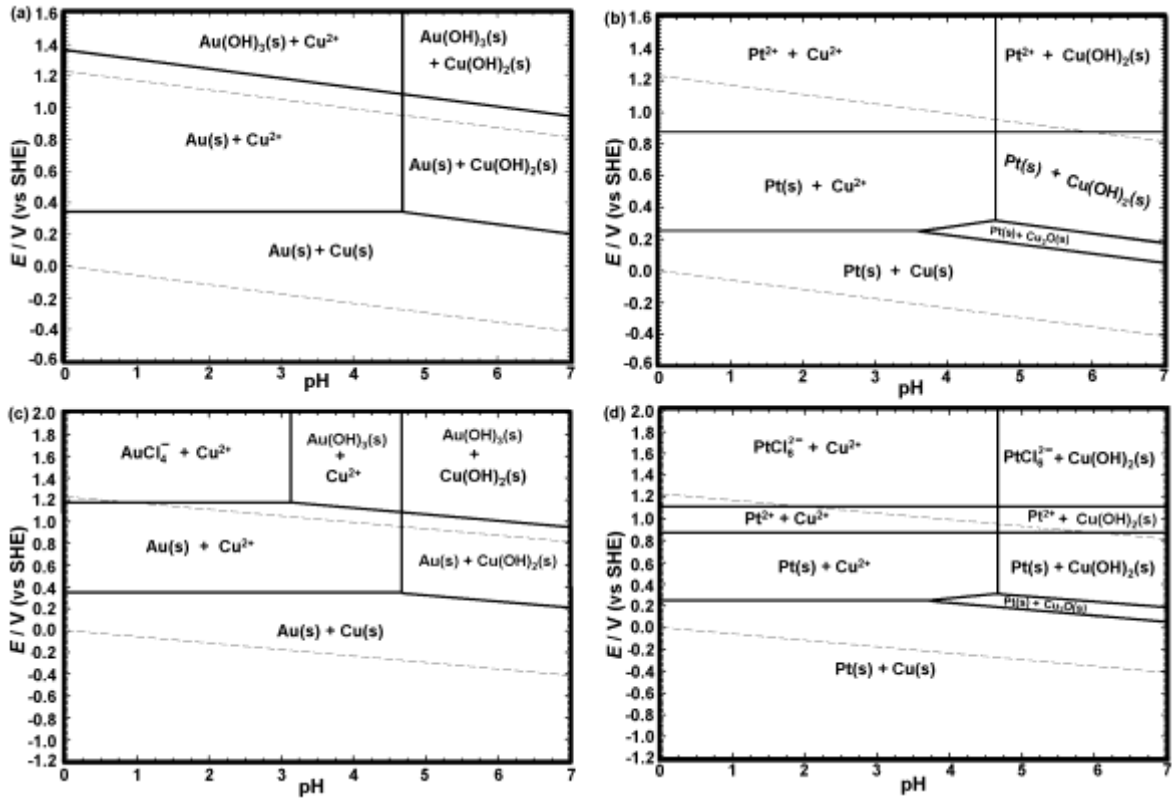


FIGURE 4

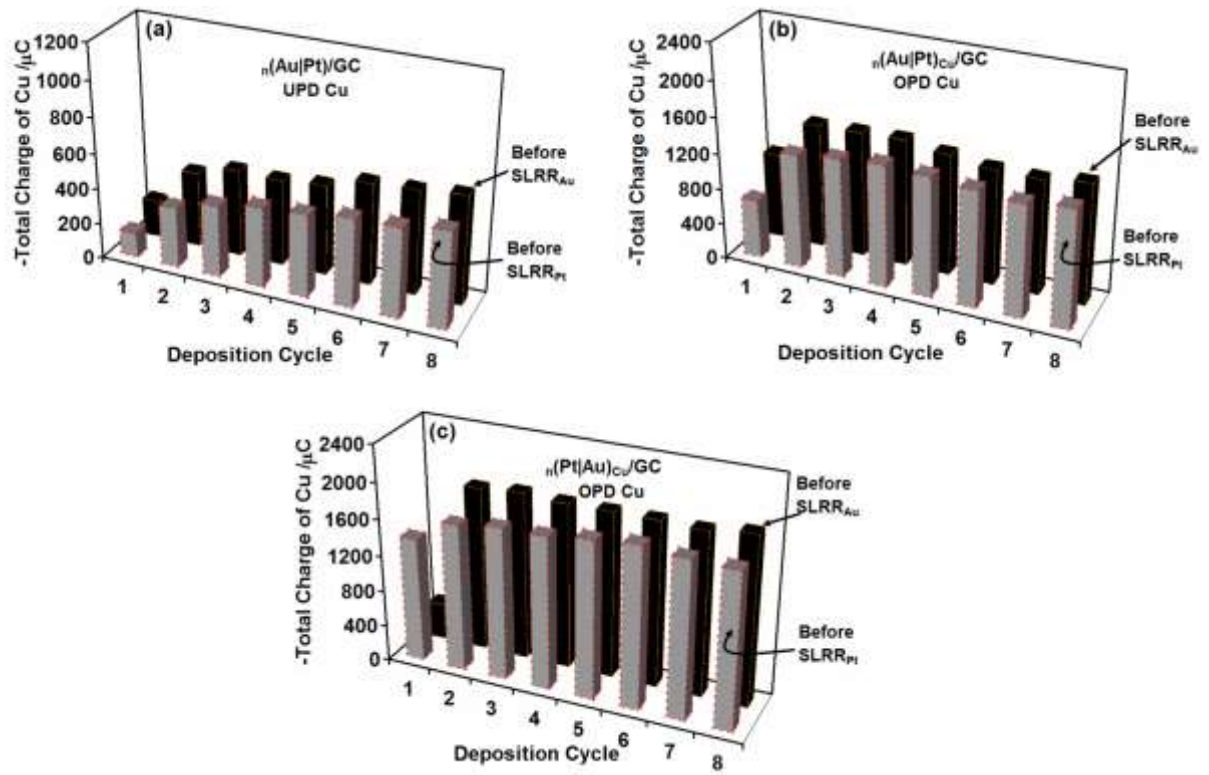


FIGURE 5

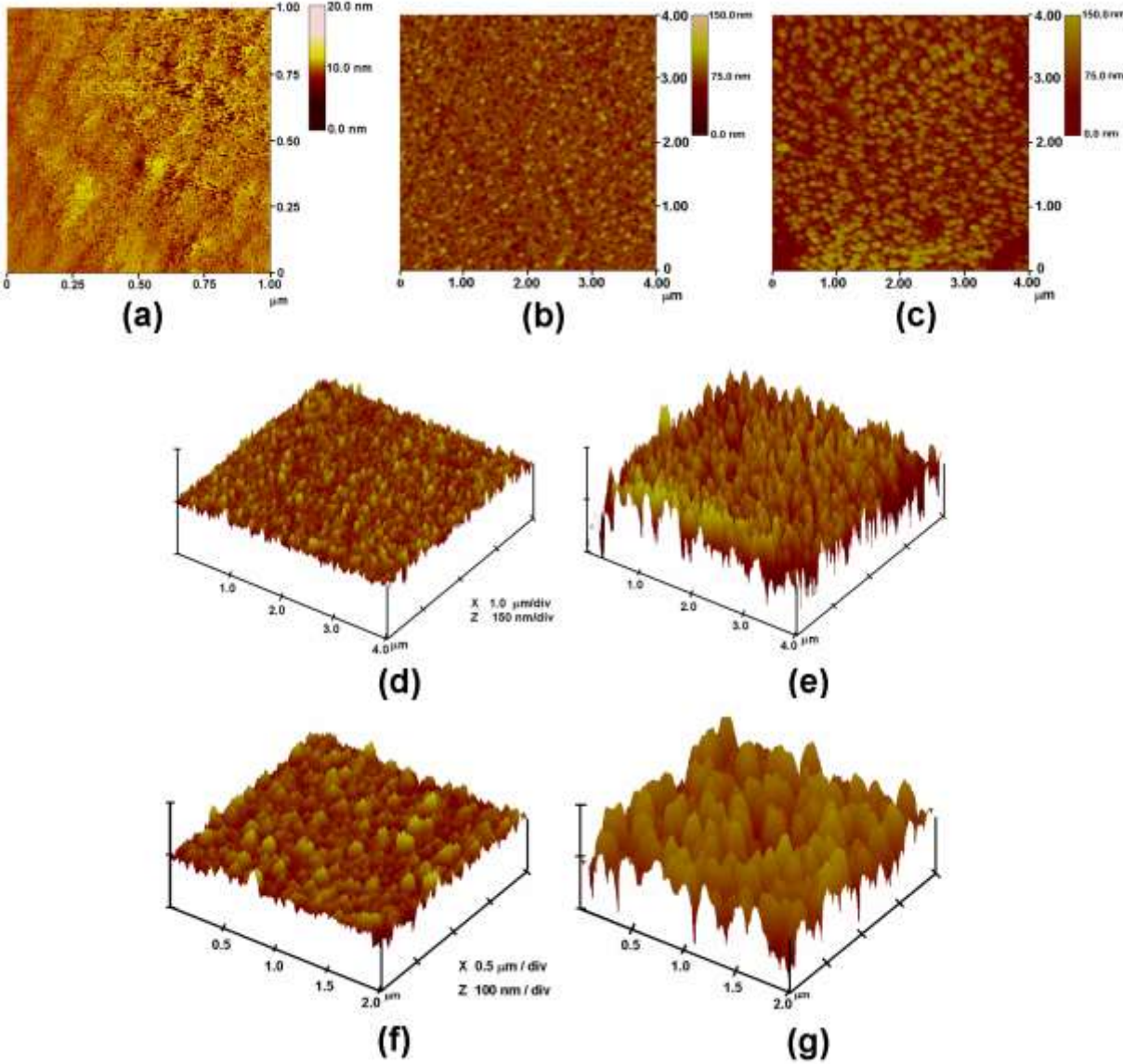


FIGURE 6

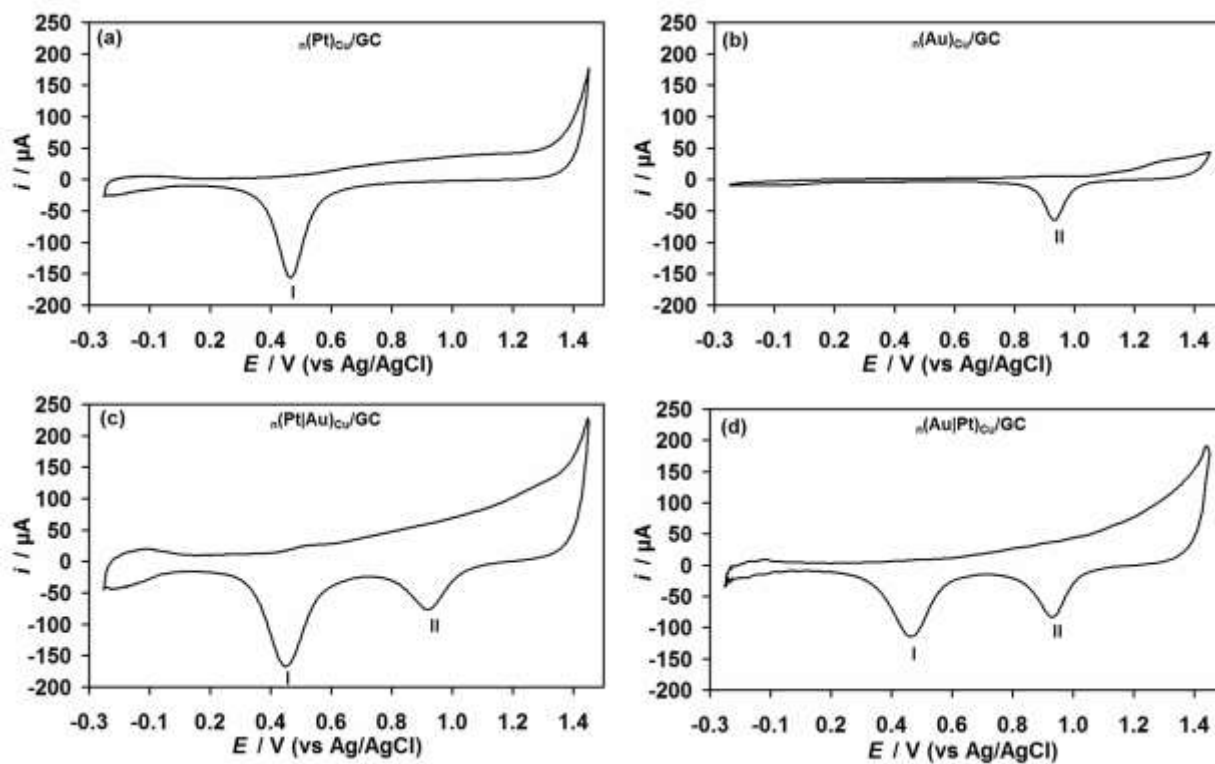


FIGURE 7

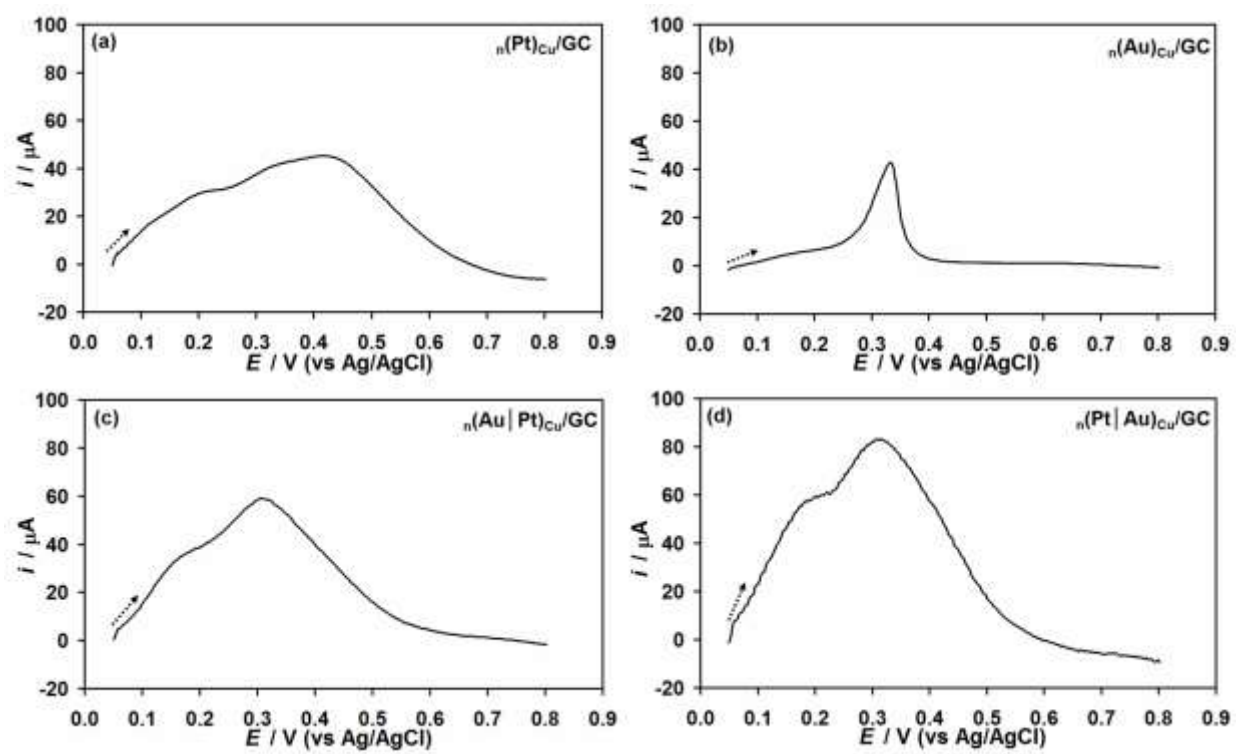


FIGURE 8

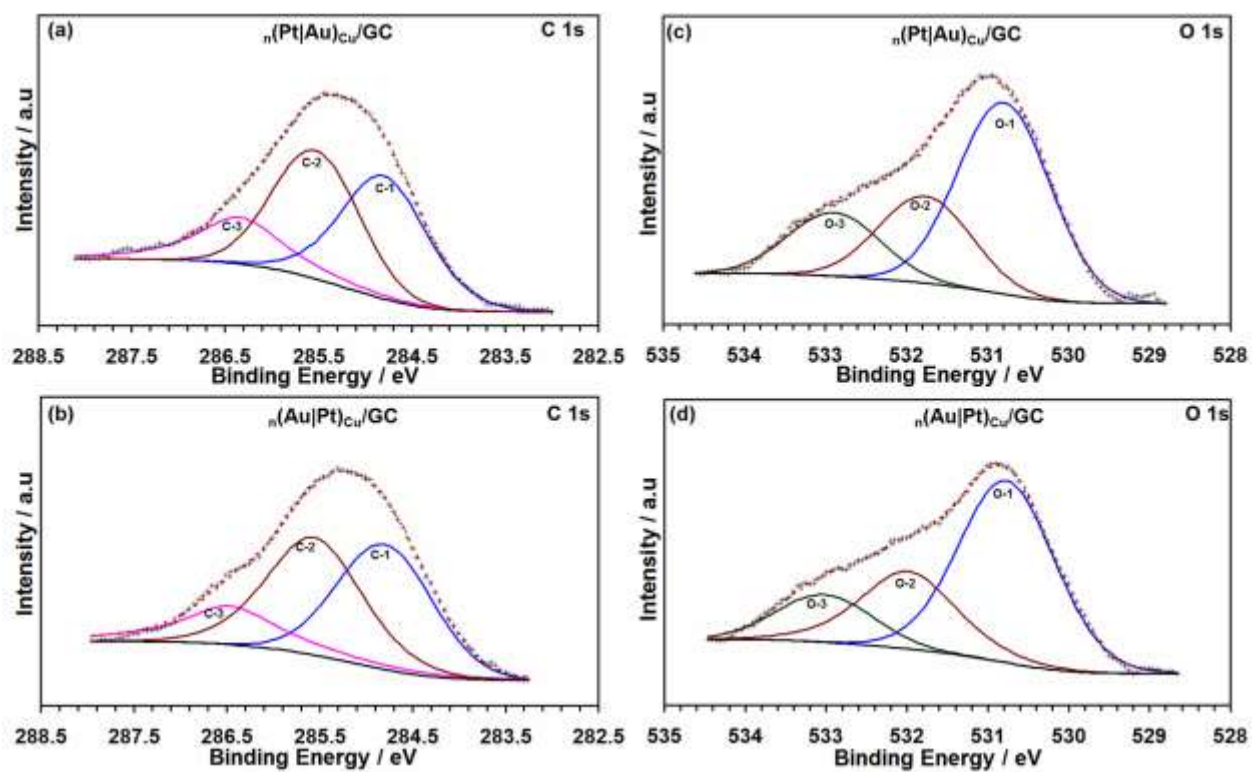


FIGURE 9

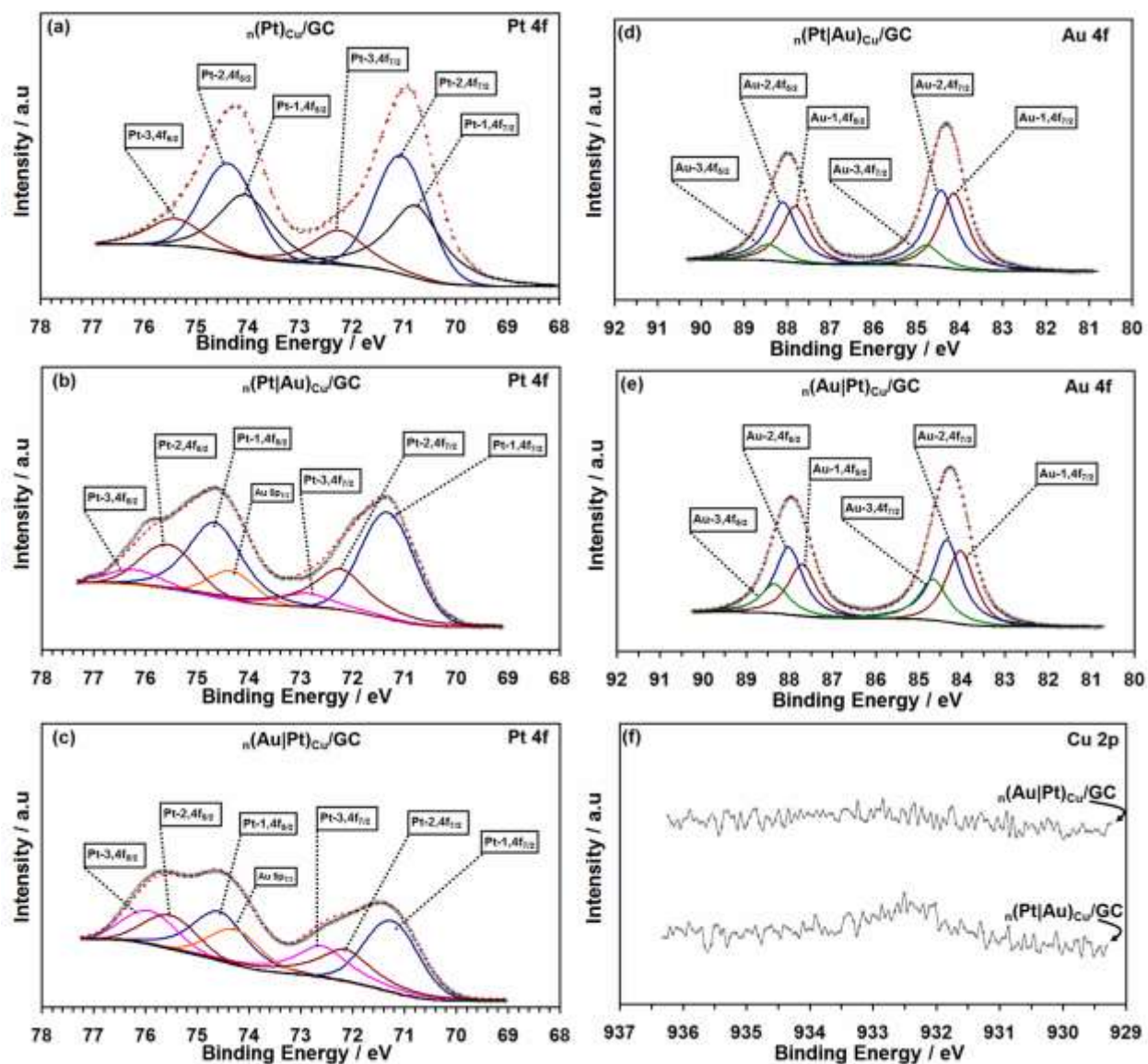


FIGURE 10

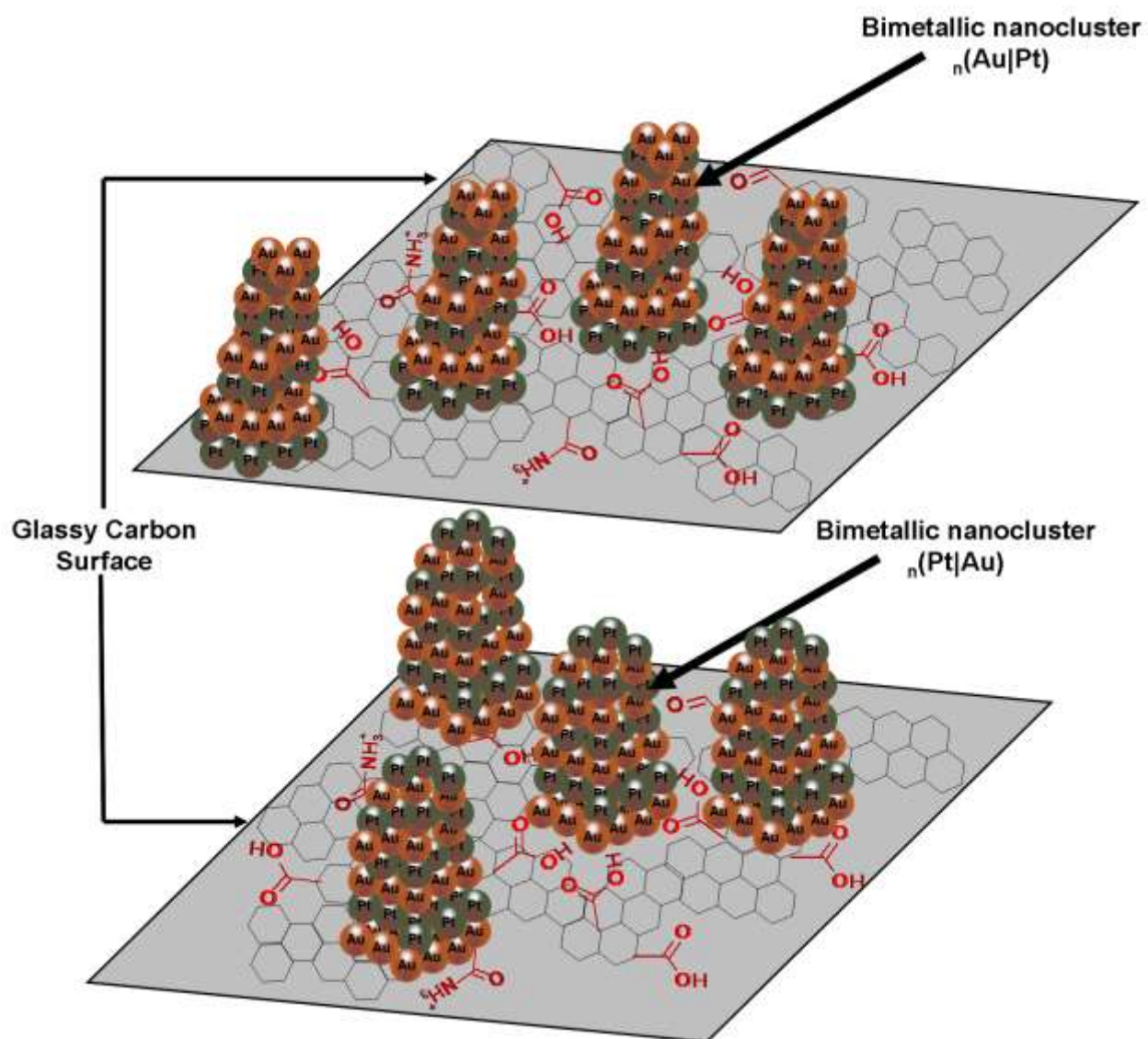


FIGURE 11

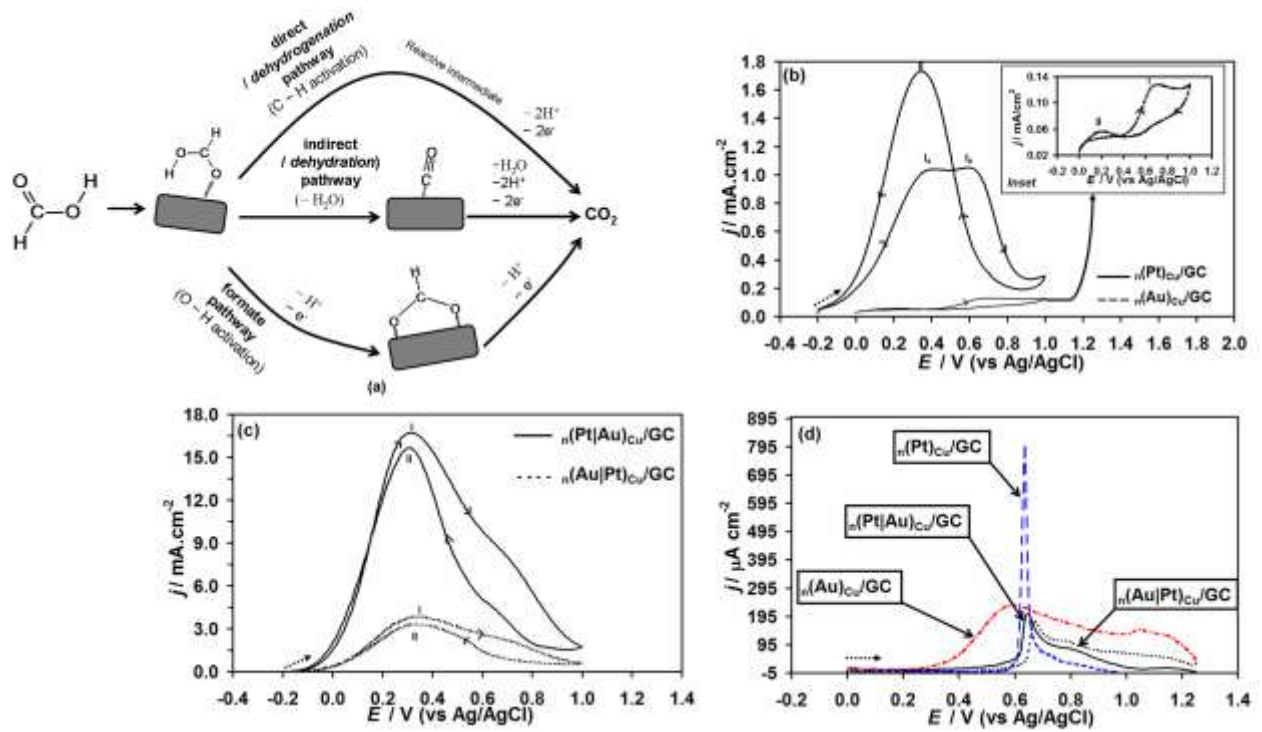


FIGURE 12

